LSST Cadence Strategy Evaluations for AGN Time-series Data in Wide-Fast-Deep Field

Xinyue Sheng,[1][*] Nicholas Ross,[2] Matt Nicholl[1]

[1] *Institute of Gravitational Wave Astronomy and School of Physics and Astronomy, University of Birmingham, Birmingham B15 2TT, UK*
[2] *Advanced Research Division, Niparo, 41 Dundas Street, Edinburgh, EH3 6QQ, U.K.*

January 19, 2022

ABSTRACT

Machine learning is a promising tool to reconstruct time-series phenomena, such as variability of active galactic nuclei (AGN), from sparsely-sampled data. Here we use three Continuous Auto-Regressive Moving Average (CARMA) representations of AGN variability – the Damped Random Walk (DRW) and (over/under-)Damped Harmonic Oscillator (DHO) – to simulate 10-year AGN light curves as they would appear in the upcoming Vera Rubin Observatory Legacy Survey of Space and Time (LSST), and provide a public tool to generate these for any survey cadence. We investigate the impact on AGN science of five proposed cadence strategies for LSST's primary Wide-Fast-Deep survey. We apply for the first time in astronomy a novel Stochastic Recurrent Neural Network (SRNN) algorithm to reconstruct input light curves from the simulated LSST data, and provide a metric to evaluate how well SRNN can help recover the underlying CARMA parameters. We find that the light curve reconstruction is most sensitive to the duration of gaps between observing season, and that of the proposed cadences, *filterdist* performs best when averaged over all LSST filters, while *cadence_drive* performs better when the poorly-sampled u band is excluded. Overall, SRNN is a promising means to reconstruct densely sampled AGN light curves and recovers the long-term structure function of the DRW process (SF_∞) reasonably well. However, we identify important systematic biases in recovering the decorrelation timescale (τ) when this is short compared to the survey cadence, showing that machine learning reconstructions may be fundamentally limited by long gaps in observations.

Key words: quasars: general – methods: statistical – surveys – software: data analysis

1 INTRODUCTION

The stochastic variability of quasars has been recognized and studied since the discovery of the AGN phenomenon[1] (Hazard et al. 1963; Schmidt 1963; Oke 1963; Greenstein 1963; Matthews & Sandage 1963; Press 1978). Observations of large numbers of quasars from wide-field surveys show changes in the UV/optical emission (e.g., Vanden Berk et al. 2004; Wilhite et al. 2005; Sesar et al. 2007) and at higher energies (e.g. Tarnopolski et al. 2020) over the course of weeks to decades. It is now understood there are several physical mechanisms that underlie the observed quasar variability, with the variable continuum UV-optical emission driven by thermal fluctuations in the active accretion disk (e.g., Shakura & Sunyaev 1973; Czerny et al. 1999; Peterson & Horne 2004; Kelly et al. 2009, 2014). Understanding the details of the AGN accretion disk is a key area of study in contemporary

astrophysics (e.g., Dexter & Agol 2011; Cai et al. 2016; Dexter & Begelman 2018; Kubota & Done 2018; Jiang et al. 2019; Jiang & Blaes 2020).

A time Continuous Auto-regressive process (CAR) has been proposed for describing the observed UV/optical AGN variability (e.g., Brockwell & Davis 2002; Kelly et al. 2009; Kozłowski et al. 2010). This was later extended to a more flexible and scalable model - the Continuous Auto Regressive Moving Average (CARMA) model (Kelly et al. 2014; Feigelson et al. 2018; Moreno et al. 2019). CARMA models are not physical models, but rather a statistical description that characterizes a time-series stochastic process. CARMA models are notated as $CARMA(p, q)$ where p gives the order of the auto-regressive (AR) process and q gives the description of the Moving Average (MA) process. The AR response can be thought of as the forecasting part, while the MA model gives the input impulse(s). The Power Spectral Density (PSD) [2], the Auto-correlation function (ACF) [3] and the Structure Function (SF)

---

[1] We use the term quasar and AGN interchangeably in the manuscript, noting that quasars are the bolometrically luminous subset of AGN.

[2] The power spectrum of the signal, describing the distribution of power across frequencies, i.e. the Fourier transform.
[3] The correlation between steps in a time series.

Variability Models:	
ACF	Auto-correlation function
ACVF	Auto-covariance Function
CARMA	Continuous AutoRegressive Moving Average
DHO	Damping Harmonic Oscillator
DRW	Damped Random Walk
PSD	Power Spectral Distribution
SF	Structure Function
LSST related:	
DDF	Deep Drilling Fields
FBS	Feature-Based Scheduler
LSST	Legacy of Time and Space Survey
MAF	Metric Analysis Framework
OpSim	Operations Simulations
PLAsTiCC	Photometric LSST Astronomical Time-Series Classification Challenge
VRO	Vera Rubin Observatory
WDF	Wide Deep Fast (survey)
Data Science terms:	
AE	AutoEncoder
BNN	Bayesian Neural Network
ELBO	Evidence lower bound
GP	Gaussian processes
GPR	Gaussian Process Regression
ML	Machine Learning
RF	Random Forest
RNN	Recurrent Neural Network
RAE	Recurrent Autoencoder
SGVB	Stochastic Gradient Variational Bayes
SRNN	Stochastic Recurrent Neural Network
SSM	State-space model
VAE	Variational Autoencoder
VRAE	Variational Recurrent Autoencoder

Table 1. Acronyms used in this paper.

[4] can all be calculated for CARMA models. Moreno et al. (2019) present a detailed CARMA handbook for optical AGN variability, discuss CARMA models and their associated statistical descriptions in full detail, and illustrate the bridge between discrete ARMA and time-continuous CARMA for fitting the irregular sampling of light curves.

The simplest CARMA model, CARMA(1,0) is the well-known "Damped Random Walk" (DRW). The DRW, and its Auto-correlation Function (ACF) and Structure Function (SF) can be expressed as:

$$d^1 x + \alpha_1 x(t) = \beta_0 dW(t) \qquad (1)$$

$$\mathrm{ACF}(\Delta t) = e^{-\frac{|\Delta t|}{\tau}} \qquad (2)$$

$$\mathrm{SF}(\Delta t) = \mathrm{SF}_\infty (1 - e^{-|\Delta t|/\tau})^{1/2}, \mathrm{SF}_\infty = \sqrt{2}\sigma \qquad (3)$$

where α_1 is the C-AR coefficient and β_0 is the coefficient of the random perturbations. In the case of AGN, x corresponds to the flux or magnitude. $W(t)$ is a Wiener process, and $dW(t)$ means a white noise process with $\mu = 0$ and variance= 1 (Kelly et al. 2014). Δt is the difference between two MJDs. There are two parameters that can be obtained from DRW to capture

the statistics of AGN variability: τ, the characteristic damping (or signal decorrelation) timescale, and SF_∞, the long-term variability amplitude.

The DRW model is a good description of long-term quasar variability and as such is often applied to data from large-area sky surveys. MacLeod et al. (2010) confirmed that a DRW model fits well for ∼9000 SDSS Stripe 82 quasar light curves, and analysed correlations between the observed variability parameters and AGN physical parameters including black hole mass, redshift, luminosity and rest-frame wavelength of emission. Suberlak et al. (2021) built on this work by adding Pan-STARRS1 photometry to the SDSS Stripe 82 data, generating light curves up to 15-years in length. They found that the variability amplitude is a stronger function of the black hole mass, and that it (and τ) has a weaker dependence on quasar luminosity than initially found in MacLeod et al. (2010).

Kozłowski (2016b, 2017) investigated systematic biases (photometric noise, etc.) in structure function measurements. They applied Monte Carlo simulations to AGN light curves, and showed that accurate estimation of DRW parameters requires the observation sampling to be at least 10 rest-frame decorrelation timescales. Kozłowski (2017) note this is because observations shorter than ∼10τ are insufficient to fully sample the PSD. Thus, due to the limited observation lengths of astronomical surveys, the estimations of DRW parameters may fall into this unconstrained region resulting in biases.

Kozłowski (2016a) reported that DRW modelling can also work well for non-DRW processes, and should not be regarded as a proxy for the physical process underlying the variable emission. On shorter timescales, other models may be more appropriate. Kasliwal et al. (2015) studied a number of *Kepler* AGN light curves (Howell et al. 2014). Compared with ground-based surveys, *Kepler* has higher photometric precision and denser observation cadences, but shorter survey length. Kasliwal et al. (2015) found that AGN with *Kepler* light curve information had log-PSD slopes steeper than than that of DRW, suggesting that the variability may be better captured by another process other than AR(1).

Combining SDSS and data from *Kepler*'s second mission, *K2*, Kasliwal et al. (2017) discuss DRW and a higher-order CARMA(2,1) model, the damped harmonic oscillator (DHO), and indicate that an overdamped DHO[5] may be a better description of the AGN Zw 229-15 (see Figures 1 and 3 from Kasliwal et al. 2017). The PSD timescale features for Zw 229-15 are also reported by Edelson et al. (2014) and Williams & Carini (2015). Kovačević et al. (2020) present a method to model AGN variability using a representation of the DHO model with Gaussian processes (GPs), and successfully detect variability due to continuum emission and (broad) line emission.

Thus, DRWs and DHOs are useful descriptions of quasar light curves. The key goal of CARMA models now is to accurately measure the model parameters from observed quasars, and use this information to study the underlying physics. We summarise the working equations for the DRW=CARMA(1,0) and DHO=CARMA(2,1) models in Table A1. Table A1 presents the differential equations, input parameters, impulse response (IR, also called Green's function), structure function

---

[4] The average change as a function of time interval.

[5] Whose impulse response moves slowly toward equilibrium.

(SF), auto-correlation function (ACF), auto-covariance function (ACVF) and power spectral density (PSD) for DRW and DHO processes. Table A2 explains all acronyms and notation.

Our ability to study AGN variability will soon be transformed by the Vera C. Rubin Observatory (VRO), conducting the Legacy Survey of Space and Time (LSST). The VRO telescope, located on Cerro Pachon in Chile, has an 8.4m (6.5m effective) primary mirror, with a 9.6 deg^2 field of view, a 3.2-gigapixel camera and six filters (*ugrizy*) covering the wavelength range 320-1050nm.

LSST will repeatedly observe millions of objects, with ≥ 825 visits for any given point in the survey footprint and a single-visit depth ≈ 24.5 mag in the *r*-band. LSST will cover the whole Southern sky, and part of the Northern sky, as part of the Wide-Fast-Deep (WFD) survey. There are also five Deep-Drilling fields (DDF; LSST Science Collaboration et al. 2009). The WFD will take about 90% observing time, with >10 million quasars projected to be identified, though the cadence strategies will have an effect on the efficiency of quasar identification (Ivezic 2016). This has motivated recent white papers from the LSST AGN Science Collaboration for estimating the influence of cadence strategies on AGN astrophysics studies[6]. Kovacevic et al. (2021b) have provided statistical proxies to measure the LSST cadence effects on AGN variability observations and Kovacevic et al. (2021a) provides two metrics: based on AGN time lag and periodicity, and on the structure function. This is complementary to Yu & Richards (2021, in prep.). Such models simulate AGN light curves ahead of the start of LSST survey operations. Analyzing recovery of parameters (including e.g., characteristic timescales, power spectra densities, and impulse responses) from the simulated data under different cadences can tell us the potential systematic bias.

With the development of large sky surveys such as SDSS and LSST, astronomy has become a data-intensive science. Consequently, there have been recent attempts to use machine learning (ML) techniques to address the data challenges set by LSST, especially for classification, forecasting and parameter estimations. For example, the Photometric LSST Astronomical Time Series Classification Challenge (PLAsTiCC) included included 175,500 simulated AGN (among other transients) to test classification algorithms (e.g. Kessler et al. 2019; Hložek et al. 2020; Boone 2019). In this paper, we aim to quantify the influence of different LSST cadence strategies on AGN time-series data, in order to see if contemporary machine-learning algorithms can effectively recover CARMA model parameters.

We implement a *stochastic recurrent neural network* (SRNN) to model quasar light curves and recover the DRW and DHO model parameters by Gaussian Process Regression (GPR). Recurrent neural networks (RNN) are a popular class of ML connectionist models for sequential modelling and have been used previously in astrophysics applications (e.g., Charnock & Moss 2017; Naul et al. 2018; Hinners et al. 2018; Muthukrishna et al. 2019; Möller & de Boissière 2020; Becker et al. 2020; Escamilla-Rivera et al. 2020; Burhanudin et al. 2021; Lin & Wu 2021). However, as noted in Yin & Barucca (2021), one limitation of RNNs is that the hidden state transition function is entirely deterministic, which can limit the RNNs

ability to model processes with high variability. Thus (and as far as we can tell, for the first time in astrophysics research), we implement the stochastic recurrent neural network, in order to recreate quasar light curves. The SRNN differs from the traditional RNNs in that the RNN hidden cells invoke a probabilistic (often Gaussian) distribution to generate a level of stochasticity that improves longer-term temporal forecasting. As such, the SRNN can be somewhat thought of as a combination of an RNN and ideas from a Variational AutoEncoder (VAE).

We have two main goals:

• To test how well the SRNN can recover and predict observations when dense or uniformly-seasonal light curves are set as inputs.

• To predict AGN behaviour during gaps between seasons in 10-year LSST-simulated light curves, and see how SRNN could help recover DRW and DHO parameters.

This paper is organised as follows. In Section 2, we describe our observational data and the methods (including DRW and DHO) we use to generate sample quasar light curves. Section 3 presents the details on the LSST Observing Strategy and associated cadences. In Section 4 we describe the Machine Learning (ML) algorithms we use to evaluate the model quasar light curves. We report our key results in Section 5 and discuss these results in the context of quasar studies and LSST in Section 6. Section 7 presents our conclusions. In Appendix A we write down the fundamental parameters and equations for the CARMA models, and in Appendix B we detail the implementation of the SRNN. We report all magnitudes on the AB zero-point system Oke & Gunn (1983); Fukugita et al. (1996) unless otherwise stated. All logarithms are to the base 10.

## 2 QUASAR DATA AND MODEL LIGHT CURVES

In this section, we give the details of our quasar data, including both observed quasars from previous sky surveys, used to provide an input set of representative statistical parameters, and the model light curves we generate. For the observed quasar data we will focus on the well studied SDSS Stripe 82 field. The key analysis codes of this section are available via a github repository.

2.1 Observed Quasars

2.1.1 SDSS Stripe 82

The Stripe 82 field (hereafter S82; Annis et al. 2014) is a ~ 300 deg^2 region of the SDSS across 22h 24m < R.A. < 04h 08m, |Dec.| < 1.27 deg, and has been observed ~ 60 times on average to search for transient and variable objects (Abazajian et al. 2009). These multi-epoch data have time-scales ranging from 3 h to 8 yr and provide well-sampled five-band light curves for an unprecedented number of quasars. Examples of quasar variability studies based on S82 photometry include Sesar et al. (2007), Schmidt et al. (2010), Ai et al. (2010), MacLeod et al. (2010), MacLeod (2012), Meusinger et al. (2011), Butler & Bloom (2011), Kozłowski (2016b) and Suberlak et al. (2021).
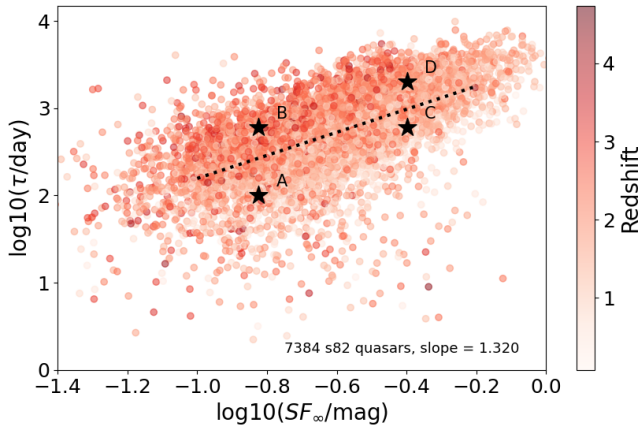
Figure 1. The SF_∞ and τ distribution of 7384 quasars in g band selected from the SDSS Stripe 82 field, with spectroscopic redshift given by point color. The dashed line is the regression line, and the four star markers represent four DRW parameter pairs, the associated light curves of which are shown in Figure 2.

For our study we will concentrate on the ∼9000 spectroscopically confirmed quasars from SDSS Stripe 82 reported in MacLeod et al. (2010)[7]. MacLeod et al. (2010) model the time variability using the DRW and measure the characteristic timescale (τ) and an asymptotic r.m.s. variability on long timescales (SF_∞). Also reported for this dataset is the binary value `edge` (if the observation is close to the field edge) and a set of probabilities: *P*like (log likelihood of a damped random walk solution), *P*noise (log likelihood of a noise solution) and *P*inf (Log likelihood of $\tau \to \infty$).

In order to have a sample of objects that have well fitted DRW parameters, we selected those with `edge` = 0, *P*like-*P*noise> 2, and *P*like-*P*inf> 0.05. We also remove objects with $\tau < 0$ or $\tau > 10^5$ days to allow convergence in τ. With these selections, the number of quasars in the sample is 7384. We plot the SF_∞ and τ distribution of these quasars in Figure 1.

2.2 Model Quasars

Our aim is to analyse the influence of survey cadence on quasar modelling in LSST. We note again that although CARMA models are not physical models, they are appropriate approximations of quasar light curve properties. As such, we simulate the light curves using a DRW and DHO implementation. We first generate 10-year light curves (consistent with LSST survey length) with dense, daily observations, which can later be sampled at different realistic cadences. The steps to generate light curves are described in the following sections.

2.2.1 DRW simulated light curves

For the DRW model, two input parameter choices are required: SF_∞ and τ, in addition to the redshift (z). To generate our model light curves, we sample the SF_∞-τ parameter space from the S82 data set MacLeod et al. (2010) shown in Figure 1. We take the values reported at a given SF_∞-τ coordinate and

parameter	values	values
	Underdamped	Overdamped
τ_{decay}	60∼200	60∼200
τ_{QPO}	7.8∼380	−
τ_{rise}	−	5.6∼38.8
ξ	0∼1	2∼5
β_0	0.0022	0.003672
β_1	0.00025	0.0257
N_{tot}	1000	1000

Table 2. DHO parameters for underdamped and overdamped cases. These values restrain the range of the real parameters, but they are not applied with fixed increments to avoid combinations that lead to unrealistic derived statistical parameters (calculated using Table A1) – such simulated cases are removed.

add a "scatter" in the range $-0.05 < \iota < 0.05$ (as determined by a random number generator) to each ordinate separately. We generate 30,000 DRW light curves parameter pairings in this manner.

The four black stars in Figure 1 are four DRW pairs, and we show their associated light curves, structure functions and PSDs in Figures 2 and 3. Given a fixed value for SF_∞ and a set rest-frame observation length, longer characteristic timescales (τ) will lead to less fluctuation. When τ is short compared with the rest-frame observing duration, the variance of the light curve will tend towards σ^2 and the estimated parameters will approach the underlying values.

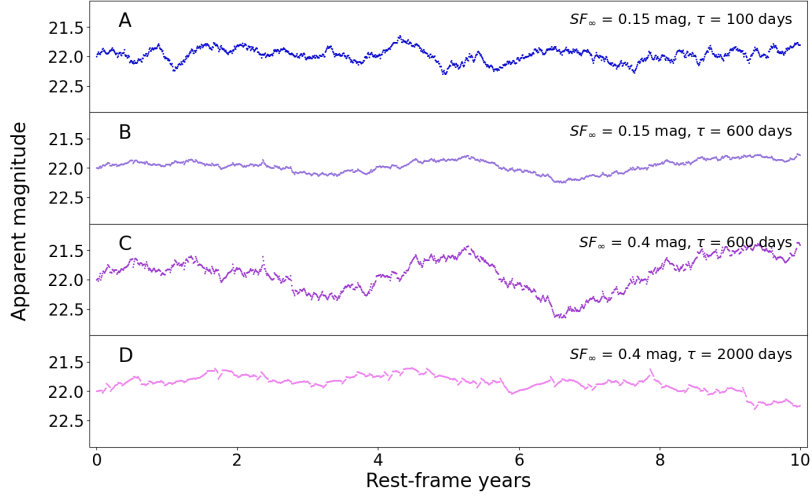### 2.2.2 DHO simulated light curves

The literature is not so comprehensive for DHO modelling of UV/optically bright AGN, though there are papers that report the PSD slopes of some quasars are not consistent with DRW (e.g., Kasliwal et al. 2015, 2017; Moreno et al. 2019). These illustrate that a more complex CARMA process might be a better model for describing quasars variability, especially for objects with weak oscillation features. As such, we build a DHO set including both 'overdamped' and 'underdamped' cases.

Five parameters are required as inputs: β_0, β_1, ξ, τ_{decay}, and τ_{QPO} (the timescale of quasi-periodic oscillations) in the 'underdamped' case or τ_{rise} (the timescale to brighten in response to an impulse) in the 'overdamped' case (See Table A2 for details). To build the light curves, the redshift and SF_∞ for each light curve are randomly sampled from the Stripe 82 distribution. τ_{decay} is set to vary from 60 to 200 days. MA coefficients β_0 and β_1 are set with constant and small values to ensure that dependent parameters remain in reasonable ranges (see Appendix A1). Additionally, we set $2 < \xi < 5$ for the overdamped case, $0 < \xi < 1$ for the underdamped case. In this way, we can calculate the corresponding C-AR coefficients α_1 and α_2 using the recipes in Table 2.

Figure 4 shows four DHO light curves, including two underdamped and two overdamped, with their Impulse Response functions. For the underdamped DHO, the Impulse Response oscillates and gradually returns to a steady state, whereas in the overdamped case, it gradually moves to its steady state without oscillation. Analogous to Figures 2 and 3 for the DRW model, Figure 5 depicts the PSD and SF for the underdamped and overdamped DHO.

Figure 2. Four light curves simulated from the DRW parameters in the SDSS Stripe 82. The mean magnitude is 22.0 mag.
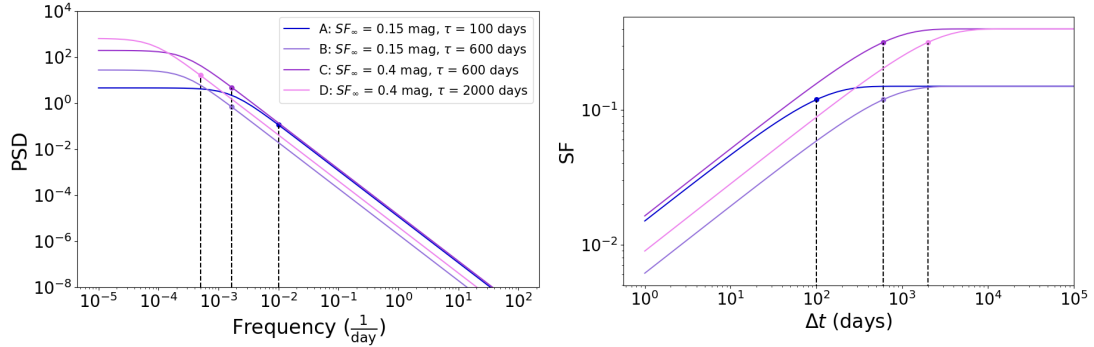
Figure 3. *(Left):* The Power Spectral Density (PSD) for the four example DRW light curves as given in Figure 2. The PSD is determined by the driving force ($\beta_0\, dW(t)$ in DRW equation). For DRW, there is only one AR coefficient β_0, resulting that slope of PSD will be flat with f^{-2} after the break point. *(Right):* The Structure Function (SF) describes the trend of standard variance of magnitude differences with Δt. The vertical dash lines correspond to τ^{-1} and τ in each graph respectively.

2.2.3 GPRs and `Eztao`

We generate the DRW and DHO light curves using the `Eztao` Python package[8], developed by Weixiang Yu. `Eztao` is a Python toolkit for conducting time-series analysis using CARMA processes. Building on work by Rybicki & Press (1995) and in particular Foreman-Mackey et al. (2017), `EzTao` uses *celerite* (a fast gaussian processes regression library) to compute the likelihood of a set of proposed CARMA parameters given the input time series.

A Gaussian process (GP) is a generalization of the Gaussian probability distribution and a Gaussian process regression (GPR) model provides uncertainty estimations together with prediction values. Gaussian processes[9] and Gaussian process regression are discussed extensively elsewhere (e.g., Rasmussen & Williams 2006). Here, we use `EzTao` to model and produce GPRs that give uncertainty estimations together with predictions for DRW and DHO light curves.

2.2.4 Colour-Redshift correlation and SF_∞

The observed colour of a quasar changes with redshift, (e.g., Richards et al. 2001). To quantify this, we select 151,362 quasars included in the SDSS DR16 Quasar catalog (DR16Q; Lyke et al. 2020) that are also in the UKIDSS (**?**) footprint. We convert from UKIDSS/WFCAM Vega Y-band to LSST AB y-band[10], and calculate the colours $(u-g)$, $(g-r)$, $(r-i)$, $(i-z)$, $(z-y)$ from redshift $z = 0.00 - 5.00$, in redshift bins of $\Delta z = 0.05$. We initially generate mean magnitudes in the g-band, and normalise the other bands using these colour relations.

Examining the SF_∞ values for 9258 S82 quasars from MacLeod et al. (2010)[11] (MacLeod et al. 2010), we find that SF_∞ is larger in bluer bands. As SDSS doesn't provide a y filter, we calculated the SF_∞ and τ ratios for the S82 quasars in 6 bands (shown in Table 3), and fix the ratio of y band $SF_\infty(y)/SF_\infty(u) = 0.61$, and $\tau(y)/\tau(u) = 1.26$.

---

[8] Eztao Python package and also on GitHub
[9] http://www.gaussianprocess.org/

[10] $mag_{\mathrm{AB}} = -2.5 \log(F_\nu) - 48.6$
[11] Available here
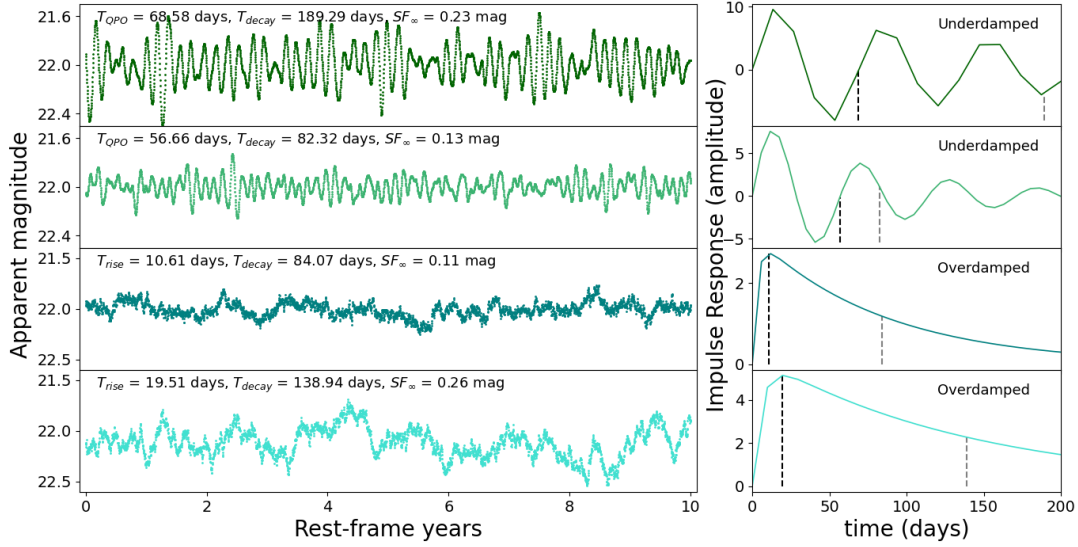
Figure 4. Four light curves simulated by DHO. Upper two are underdamped and lower two are overdamped cases, followed with their Impulse Response. For underdamped IR, the black dash line means τ_{QPO} and grey line means τ_{decay}. In overdamped IR, the black line corresponds to τ_{rise}, and grey τ_{decay}.

(a) Power Spectra Density

(b) Structure Function
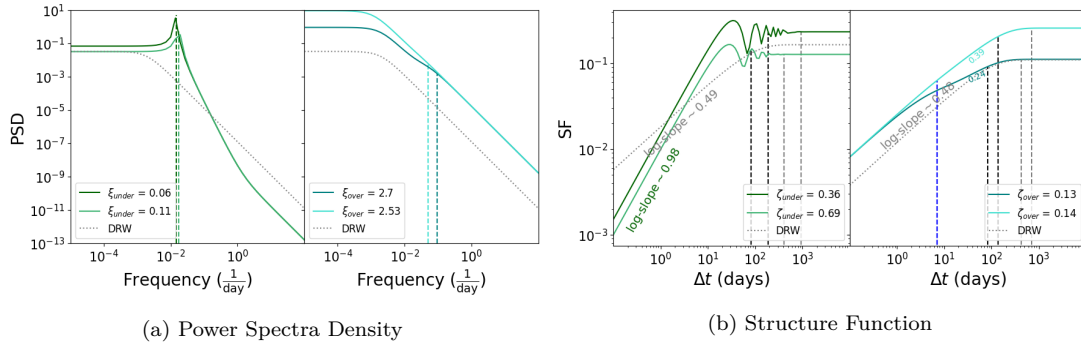
Figure 5. PSD and SF for 4 DHO light curves with underdamped and overdamped cases. The LHS (RHS) of each subplot represent the PSD and SF for underdamped (overdamped) DHO. For Figure 5a, ξ means the damping ratio. The vertical dash lines represent $1/\tau_{\mathrm{QPO}}$ (left), and $1/\tau_{\mathrm{rise}}$ (right) respectively. For Figure 5b, ζ means the ratio of $\tau_{\mathrm{QPO}}/\tau_{\mathrm{decay}}$ (left) and $\tau_{\mathrm{rise}}/\tau_{\mathrm{decay}}$ (right). The black and grey dash lines depict τ_{decay} and $5\tau_{\mathrm{decay}}$ respectively. It is worth noting that when Δt is equal to $5\tau_{\mathrm{decay}}$, the structure function has been steadily close to SF_{∞}. The blue dash line on the right plot represents τ_{blue}, where the overdamped SF slopes just decrease (Moreno et al. 2019).

band	u	g	r	i	z	y
SF_{∞} ratio	1	0.88	0.75	0.66	0.63	0.61
τ ratio	1	1.29	1.51	1.28	1.26	1.26

Table 3. The ratios are the mean values of (SF_{∞} or τ in a given band) over mean (SF_{∞} or τ in the u-band) for the Stripe 82 quasar data.

2.2.5 LSST Photometry and Photometric Error

Here we note the expected photometric performance of LSST, and tie this to our synthetic model quasar light curves. Detailed LSST performance metrics are given in Ivezić et al. (2019, Section 3.2.1), and the expected photometric error in magnitudes for a single visit can be written as:

$$\sigma^2_{\mathrm{LSST}} = \sigma^2_{\mathrm{sys}} + \sigma^2_{\mathrm{rand}} \qquad (4)$$

$$\sigma^2_{\mathrm{rand}} = (0.04 - \gamma)x + \gamma x^2 (\mathrm{mag}^2) \qquad (5)$$

where σ_{sys} and σ_{rand} are the systematic and random photometric error respectively, $x \equiv 10^{0.4(m-m_5)}$ and m_5 is the typical 5σ depth of point source at zenith for each visit. Given the fact that the calibration system and procedure are set to maintain $\sigma_{sys} < 0.005$ mag, we assume $\sigma_{sys} = 0.004$ mag. γ is a band-dependent parameter. Following Table 2 in Ivezić et al. (2019), we set $\gamma_u = 0.038$ and $\gamma_{g,r,i,z,y} = 0.039$. LSST OpSim provides the m_5 for each visit in a proposed cadence strategy. In this way, for one original simulated photometric value, a photometric error is randomly selected from a Gaussian distribution, with mean equal to 0 and variance equal to σ^2_{LSST}.

2.3 Model Light Curve data products

Following the steps above, we generate a dataset containing light curves generated from the DRW and DHO models. We simulate 200 objects from each of the DRW, DHO-overdamped and DHO-underdamped models, and for each object, light curves in 6 bands are generated, with one observation per day. The mean magnitude, SF_∞, and τ follow the restrictions detailed in Section 2.2.

These light curves will be used in Section 4 for the SRNN analysis, and are also made available to the community[12].

3 SIMULATED AGN WITH LSST CADENCES

In this section we present the light curves of the simulated quasars and how they will be observed using realistic LSST observing Cadences. The survey strategy and cadence choices for LSST are described in detail by Jones et al. 2021 (LSST Project Science Team Note 051). The LSST Survey strategy is designed to fulfill the core science goals (which can be found at Science Requirements Document). The baseline design elements for the WFD are: *(i)* cover at least 18,000 deg^2; *(ii)* average 825 visits per field, in all filters, over 10 years, and *(iii)* obtain same-night, same-field re-visit "pairs".

Within these bounds, several key characteristics that will define the main WFD survey remain to be determined, including: how the survey area is defined (`footprint`, for short); how often each WFD field should be re-visited (`cadence`) – both for intra- and inter-night visits; and what are the optimal filter distributions for the WFD fields (`filter`) and the optimal intra-night filter pairs for WFD revisits (`colours`).

3.1 LSST cadence strategies

The LSST is a complex survey with numerous science drivers. To this end, nearly 200 simulations of observing strategy have been generated that look into how different observations will drive the science goals and various metrics (see e.g., Lochner et al. 2021).

The survey strategies are summarised online[13] and we use the v1.7 version[14]. There are "families" of observing strategies, with members of each family having related traits, e.g. the `visit_time` family are simulations examining the effect of the length of the individual visits, and the e.g. `u_long` family are simulations bearing on the length of the u-band exposure time.

The LSST Operations Simulator (OpSim) is designed to simulate LSST observing strategies over the 10-year survey, and different strategies have been tested to consider different scientific requirements (LSST Science Collaboration et al. 2017). Since this work is concerned with the global performance of machine learning neural networks in recovering quasar light curve parameters, we decided to focus on five strategies (out of the over 190 available): a baseline and four different families. We do note that the LSST collaboration readily provide the

cadence simulations, and we are providing our analysis codes, so studies with other observing strategies are easily produced.

The five survey strategies we focus on are:

- `baseline_nexp2_v1.7_10yrs`, which we call *baseline* for short. This is the baseline WFD footprint, with the default observing behavior having visits of 2×15sec exposures.
- `u_long_ms_60_v1.7_10yrs`, which we call *u-long* for short. Observations in the u-filter are taken as single snaps, and we test increasing u-band exposure times. The cadence we choose has 1×60sec, with the number of u-band visits left unchanged, resulting in a shift of visits from other filters to compensate for the increase in u-band observing time. With quasars being bright in the UV/optical, we are keen to seen if additional u-band exposure improves the recovery of light curve parameters.
- `filterdist_indx4_v1.5_10yrs`, which we designate *filterdist* for short. The aim is to evaluate the impact of changing the balance of visits between filters, where again we choose a "u-band heavy" cadence as our focus is on AGN.
- `cadence_drive_gl200_gcbv1.7_10yrs`, which we designate *cadence_drive* for short. This investigates the impact of reducing the gaps between g-band visits over the month, essentially down-weighting the lunar cycle. This aims to avoid long gaps in g-band coverage with the goal to improve transient discovery and variable characterization for longer timescale objects which require bluer filter coverage (such as AGN and SNe). Our chosen cadence has 200 fill-in g-band visits each night in a contiguous area.
- `rolling_scale0.9_nslice3_v1.7_10yrs`, which we designate *rolling* for short. A rolling cadence is where some parts of the sky receive a higher number of visits during an 'on' season, followed by a lower number of visits during an 'off' season. During the first 1.5 years and the final 1.5 years of the WFD survey, half the sky is covered uniformly, allowing for better proper motion coverage. This leaves 7.0 years for 'rolling' observations, with the benefit that transient and variable phenomena are better observed, at the cost of each of the middle 7 years will have no uniform survey coverage. Full details of the rolling cadences are given in Yoachim et al. 2021.

We summarise the salient details of these strategies in Table 4.

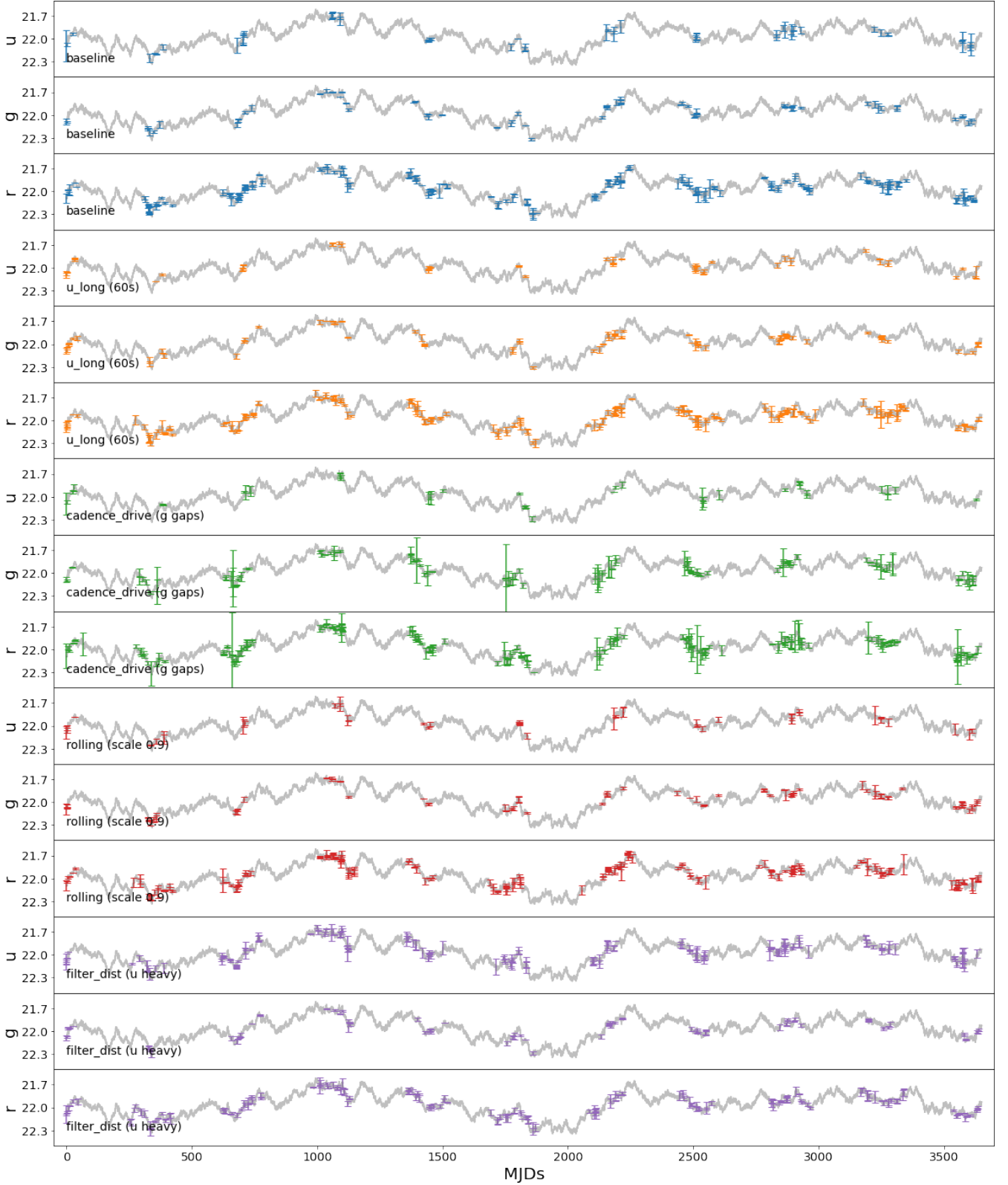### 3.2 Light curve with five cadence strategies

We selected and tested the LSST cadence simulations on the SciServer and use the Metrics Analysis Framework (MAF; Jones et al. 2014), to analyse the OpSim simulated surveys. We chose several sky positions in WFD fields, and assume that each position corresponds to a quasar object. Given a set of DRW/DHO parameters, a mean magnitude, a chosen band and an LSST cadence, we provide a `QuasarMetric` to return a realistic LSST-cadence light curve with MJDs, magnitude and magnitude error. This metric can be used for any WFD survey strategy, so will be beneficial for future AGN light curve analysis.

Figure 6 presents a DRW-simulated light curve as observed under five cadence strategies. In the next section, we will discuss the influence of different strategies on quasar modelling with GPR and machine learning.

Figure 6. Identical DRW-simulated light curve ($SF_\infty = 0.17$, $\tau = 100$, $z = 0$) at position RA = 0, Dec = -10, under five different cadence strategies. The grey light curve is the original one with dense observations. For each cadence strategy, u, g, r bands' cadences are selected. For *u_long* strategy with 60s exposure time in u band, the photometric error is much smaller than others. However, *cadence_drive* bearing reducing g band gaps, some of its observations have large noise. The *rolling* cadence with scale 0.9 shows apparent trend in seasons after around 1000 days - the number of observations in the prior season grows and downs in its next season. Compared with *u_long*, *filterdist* for u band heavy has more overall visits in u band.

	Area with > 825 visits	Unextincted Area	Nvisits total	Median	Median Nvis						Briefly desc
					u	g	r	i	z	y	
`baseline`	17982.70	15174.43	2045493.0	888.0	55.0	79.0	189.0	190.0	170.0	180.0	Baseline
`u_long`	18112.80	15011.61	1986422.0	915.0	51.0	76.0	183.0	184.0	166.0	175.0	*u* 1x60s
`filterdist`	19886.22	14974.68	2221366.0	1057.0	166.0	91.0	206.0	205.0	188.0	195.0	*u* heavy
`cadence_drive`	17996.97	14996.50	2046411.0	893.0	46.0	115.0	194.0	179.0	160.0	170.0	Add g, limit 200/night, contiguous
`rolling`	17960.88	15051.89	2048229.0	889.0	54.0	78.0	189.0	190.0	170.0	181.0	0.9 strength, 3 band

Table 4. Brief overview of the five LSST cadence strategies used in our study. Details are taken from the Jupyter Notebook nbviewer.jupyter.org/github/lsst-pst/survey_strategy.

parameter	description
g_{ϕ_a}	represents one GRU neuron function in general in the 'a' layer
$\boldsymbol{h}_t$	hidden state
$\boldsymbol{x}_t$	input data
$\boldsymbol{x}_{1:T}$	$= \{\boldsymbol{x}_1, \boldsymbol{x}_2, ...\boldsymbol{x}_T\}$ is a temporal sequence
$\boldsymbol{y}_t$	target variable
$\boldsymbol{z}_t$	latent random variable
θ	the parameters set of $\{\theta_y, \theta_h, \theta_z\}$
p_θ	Generative distribution
q_ϕ	Inference distribution
$\mathbb{E}$	the Expected Value operator
$\mathcal{L}$	marginal log-likelihood function
$\mathscr{F}$	evidence lower bound (ELBO)
D_{KL}	the Kullback-Leibler divergence

Table 5. SRNN nomenclature and notation.

4 STOCHASTIC RECURRENT NEURAL NETWORKS

In this section we give a very high-level theoretical outline of stochastic recurrent neural networks. We describe the SRNN architecture for our investigations, and how we implement the SRNN in practice. We note Fabius & van Amersfoort (2015), Chung et al. (2016), Fraccaro et al. (2016), Schmidt & Hofmann (2018) and in particular the notation from Yin & Barucca (2021) – as given in Table 5 – as important influences in what follows.

4.1 SRNN high-level overview

Fraccaro et al. (2016) propose the idea of propagating stochasticity in a latent state representation with recurrent neural networks. They stack a state space model on deterministic RNNs to achieve a stochastic and sequential generative model and a structured variational inference network, which produce the output sequences and provide the model's posterior distributions, respectively.

This algorithm is particularly suitable for CARMA modelling as there are stochastic features, and CARMA can be represented as a format of state space models. As such, here we applied SRNN to ingest AGN light curves with different LSST cadences and bands, and output modelled light curves with denser observations. The implementation of our SRNN,

with the Generative Model and the Inference Model that we use in our study, is outlined in Figure 7.
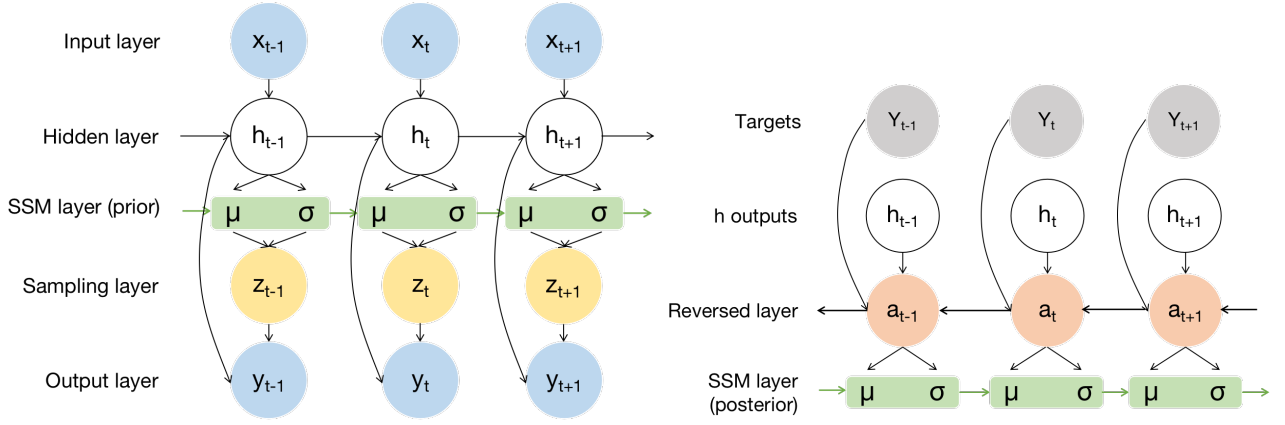
4.1.1 Generative Model

The role of the generative model is to establish probabilistic relationships between the target variable $\boldsymbol{y}_t$, the intermediate variables of interest $(\boldsymbol{h}_t, \boldsymbol{z}_t)$, and the input $\boldsymbol{x}_t$. Within the Generative Model, a key part of how the RNN becomes an SRNN is the State space model (SSM). Inside a 'classical' RNN, the evolution of the hidden states $\boldsymbol{h}$ is governed by f, a non-linear transition function: $\boldsymbol{h}_{t+1} = f(\boldsymbol{h}_t, \boldsymbol{x}_{t+1})$, where $\boldsymbol{x}$ is the input vector. For an SSM however, the hidden states are assumed to be random variables, $\boldsymbol{z}_t$. In our model, the SSM layer latent states are Gaussian distributions. The input of the next layer is randomly sampled from these distributions, thus providing the stochastic features. The key design of our model is to stack an SSM layer on the last GRU $\boldsymbol{h}$ layer (Fig. 7, left).

Given the fact that CARMA can be written as developing Gaussian distributions over timesteps, the SSM layer is expected to present similar functions for generating the output sequences. In this way, the model can learn both the long-term dependency within a sequence, as well as the stochastic features of the input sequence. Combining the non-linear gated mechanisms of the RNN with the stochastic transitions of the SSM creates a sequential generative model that is more expressive than the RNN and better capable of modelling long-term dynamics than the SSM. Figure 7(a) shows the architecture of the generative model.

4.1.2 Inference network

The second part of the SRNN is the inference network. Here, the prior distributions in the generative model learn from the posterior distributions by Kullback-Leibler divergence (Kullback & Leibler 1951). While training, the generative model and inference network are both implemented, and learn from the backpropagation.

Figure 7(b) outlines the inference model architecture. For each step, latent states a_t are fed with the combinations of $\boldsymbol{y}_{1:T}$ and $\boldsymbol{h}_{1:T}$, so it has the information of the future timesteps from target sequences as well as previous steps' information from the last h layer in the generative model. In order to let posterior distributions contain the information from the future steps, the RNN layer is reversed in the time dimension.

Figure 7. *(a)* The architecture of the generative model (*left*). The inputs layer is connected with a hidden layer (called $\boldsymbol{h}$), which can be a GRU or LSTM layer. There could be multiple $\boldsymbol{h}$ layers, and in this diagram we only show one. A State-Space model (SSM) layer is interlocked with the last $\boldsymbol{h}$ layer, represented by prior Gaussian distributions N_{prior} in the diagram. Note that the SSM layer is implemented by two GRU layers in the programs, producing $\mu_{(p)}$ and $\log \sigma^2_{(p)}$ respectively. A sampling layer is used for randomly sampling a variable from each Gaussian distribution at each step. The output of the sampling layer is further combined with the output of the last $\boldsymbol{h}$ layer, and passed to the output *Dense* layer, to generate output sequences. *(b)* Inference network. This is for providing the posterior Gaussian distributions. The target output sequences are combined with the **output** of the last $\boldsymbol{h}$ layer (also in the generative model), and they are delivered to a **reversed** GRU layer, called $\boldsymbol{a}$. In this way, the output of the $\boldsymbol{a}$ layer at each step contains the information both from its future steps (from the target) and its previous step (from $\boldsymbol{h}$). Furthermore, a SSM layer is stacked on the $\boldsymbol{a}$ layer, producing the posterior $\mu_{(q)}$ and $\log \sigma^2_{(q)}$ for each step, which is compared with the priors by calculating the KL Divergence. During training, this divergence is considered and works with the negative log-likelihood to minimize the whole loss function.

4.1.3 Loss function

Initially, we wish to maximise the marginal log-likelihood function $\mathcal{L}$, where $\mathcal{L}(\theta) = \sum_i \mathcal{L}_i(\theta) = \log p_\theta(y_{1:T}|\boldsymbol{x}_{1:T}, z_0^i, d_0^i)$. However, the random variable $\boldsymbol{z}_t$ in the non-linear SSM cannot be integrated out analytically (see e.g. Kingma & Welling 2014, Section 2.1). Therefore, we instead aim to maximise the evidence lower bound (ELBO, also known as the variational lower bound) given as $\mathcal{F}$, with respect to the generative model parameters θ and an inference model parameter, ϕ. Thus, the objective function of our stochastic RNN is $\mathcal{F}(\theta, \phi)$, given in Appendix B1. In practice, minimising the loss function is more intuitive and convenient for implementation. Therefore, we present our loss function Equation 6, which can be derived from ELBO.

$$
\begin{aligned}
\mathcal{L} &= NLL + D_{\text{KL}_i}\left(Q(\text{z}) \parallel P(\text{z})\right) \\
&= \frac{1}{N_{lc}} \sum_i^{N_{lc}} \sum_t^{N_T} ([(m_{\text{target}_t} - m_{\text{rec}_t})^2 - m^2_{\text{error}_t}] \\
&+ \log \frac{\sigma_{p_i}}{\sigma_{q_i}} + \frac{\sigma^2_{q_i} + (\mu_{q_i} - \mu_{p_i})^2}{2\sigma^2_{p_i}} - \frac{1}{2})
\end{aligned}
\tag{6}
$$

This is formed from the negative log-likelihood and Kullback-Leibler divergence (D_{KL}) (Kullback & Leibler 1951) of the prior and posterior distributions of $\boldsymbol{z}$. Q, P correspond to the approximate posteriors in the inference network and priors in the generative model, respectively. Furthermore, the magnitude errors are considered in the loss calculation. N_{lc} is the number of light curves per loss calculation. N_T means the length of each light curve. $m_{\text{target},t}$ means the t-th observation of the target light curve, and m_{rec_t} means the t-th observation of the reconstructed light curve by SRNN. m_{error_t} represents the magnitude error in the t-th observation of the

LSST-cadence light curve (also the input light curve), with 0 for vacant observations.

4.2 Parameter Configuration

Our SRNN is built using the open-source software machine learning library TensorFlow (`tf`), with *Keras* as the backend. We used *Google Colab* as the computing platform, and chose the GPU P100 nodes option.

For the generative model, we set one bidirectional GRU $\boldsymbol{h}_t$ layer with 32 neurons, followed by two bidirectional GRU layers - for the μ_z and $\log \sigma$ priors - with 32 neurons for each layer. All layers apply the default hyperbolic function tanh as the activation function. We add a 'Bidirectional' wrapper to each GRU layer as we found during testing it increased the accuracy of the light curve reconstruction. For the inference network, similarly, there are three bidirectional GRU layers with 32 neurons, corresponding to $\boldsymbol{a}_t$, the posterior μ_z, and $\log \sigma$, respectively. The dimension of the inputs includes magnitudes y (and magnitude errors y_{err} for DRW and DHO overdamped cases). The outputs are the dense light curves, with the observation length identical to the input sequences.

As the goal of applying SRNN is to model the **whole** light curves, including those dates where there are no observations, it is necessary to discuss how to deal with these vacant timesteps. Our solution is: For each dimension, the value is first reduced by its mean values, and then zeros are added for those time steps where the observations are vacant. In other words, we preprocessed those vacancies with the mean values. As RNNs do not allow *NaN* values included in inputs, adding zeros can provide these vacancies with initial values. During training, SRNN is expected to learn the correlations between steps and predict the corresponding values for these vacancies. As such, adding zeros has less physical meaning, but more for satisfying RNNs' input rules. After multiple experiments, we

proved that this design does not hurt the modelling process too much. However, when the vacant period is too long, the predicted values will move close to the mean values[15].

We chose the *Adam* Optimizer (a stochastic gradient descent method derived from adaptive moment estimation) with a learning rate $r = 5 \times 10^{-3}$, $\beta_1 = 0.900$, $\beta_2 = 0.999$ and $\epsilon = 1 \times 10^{-7}$. The batch size is 128 per training epoch, and the maximal training epoch number is 300. `tf.keras.callbacks.EarlyStopping` is also applied with the patience set to 3 in order stop training if the loss function is no longer decreasing.

4.3 Dataset and Training plan

The output from the SRNN are light curves. To see how the SRNN performs in 'ideal' circumstances, we input a dense and uniformly sampled light curve with 3650 points (a daily observation for 10 years) to the SRNN, and target a similarly dense light curve as the output. The training data involve 7200 light curves, and test data involve 1800 light curves.

To predict the light curve during seasons in the 10-year LSST-simulated light curves, and see how SRNN could help recover the CARMA DRW and DHO parameters, light curves based on the five considered LSST cadences are also fed as the input of the SRNN, and dense light curves will be the targets. The SRNN is expected to learn the trends between seasons. In this instance, the training data involve 14,400 light curves, and the test data are 3600 light curves.

We also want to predict future observations based on observed light curves, and again see how the SRNN could help recover DRW, DHO parameters for light curves with shorter duration. As such, we shortened the length of dense and LSST-cadenced light curves to 6-9 years, and let SRNN to predict the next 1-4 years' light curves.

For both the LSST light curves as well as the SRNN predicted daily light curves, we apply the GPR method (Section 2.2.3) to measure CARMA parameters. We note, GPR is only one method to estimate the CARMA parameters of the light curves; it is not as accurate as MCMC, but more efficient.

5 RESULTS

After generating the model light curves in Section 2 and simulating observations through the LSST cadences as discussed in Section 3, we use the SRNN described in Section 4 to reconsruct the full light curves and calculate CARMA model parameters. In this section, we report the results.

---

[15] We also test to fill in these vacancies with other values. For example, making a straight line between neighboring observations, starting with the previous observation and ending with the latter one, and then filling in the vacancies with the corresponding values on the line. However, this harms SRNN's predictions for their true values. We also tested to add a Masking layer after the input layer, to prevent SRNN from considering these added zeros. This design dramatically slows down the training process, and the predictions are not as good as the architecture without Masking.
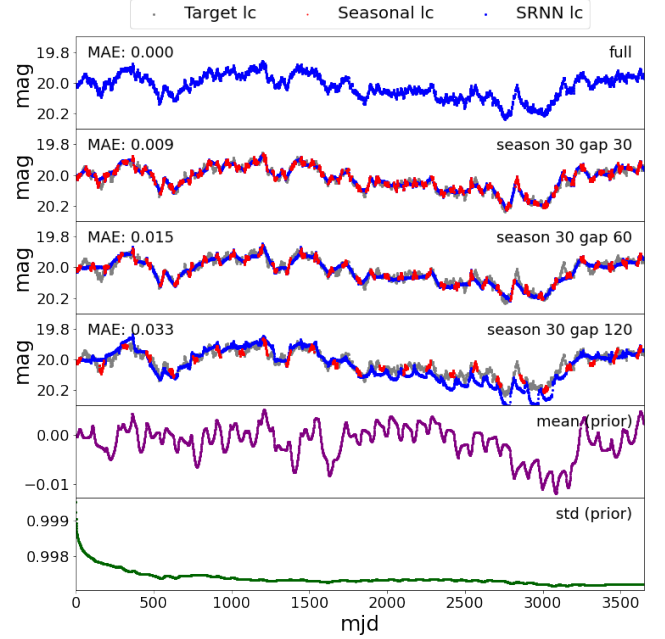
Figure 8. Multiple SRNN modellings for one DRW process ($SF_\infty = 0.1$ mag, $\tau = 307$ days) with different uniformly-designed cadences. In this experiment, the magnitude errors are set to zero for simplicity. the upper five rows correspond to input light curves with different cadences, which is labeled on the top right of each panel respectively. The input light curves are shown in red, modelled light curves by SRNN are shown in blue, and the grey means the full light curves (10 year's observation length; one observation per night). The MAE (Mean Absolute Error) between the model light curve and the target light curve is calculated for each case and displayed in the upper left corner. The last two rows show the mean and standard deviations of the Gaussian prior distributions used by one example neuron (of the many that contribute in each time step) in the state-space model layer, from which the random variable z_t is sampled (Figure 7). The case shown is for the input light curve with 'season 30, gap 120' cadence.

5.1 Light curve modelling

5.1.1 Full and uniform-seasonal light curve modelling

Fig 8 shows results of SRNN modelling for one DRW light curve ($SF_\infty=0.1$mag, $\tau=307$days) under different samplings. We test four example samplings: the light curve can be fully sampled, or have observation gaps of 30, 60 or 120 days in-between 30 days of observations.

These examples illustrate that the longer the gaps in observations, the lower the accuracy of the model and the larger the MAE. From the plot it can be seen that the SRNN is able to predict the overall trend of each gap, which is similar to its real values. It also can simulate the stochastic characteristics of the sequence, by randomly sampling from Gaussian priors (the mean and std shown in lower two panels) for each step.

5.1.2 LSST light curve modelling

For LSST-cadence light curves, it is harder for the SRNN to learn the correlations between each timestep, as the cadences are often not uniform and have longer intervals. The SRNN is
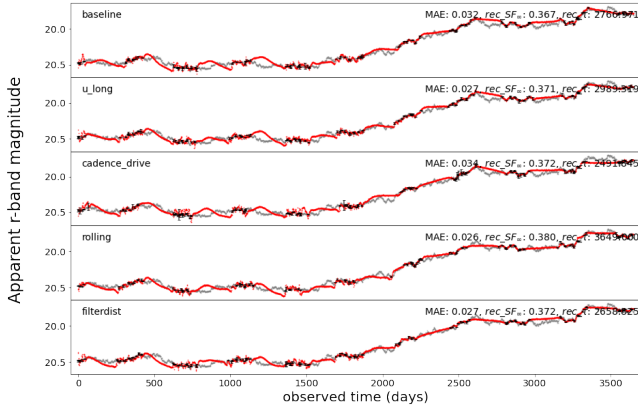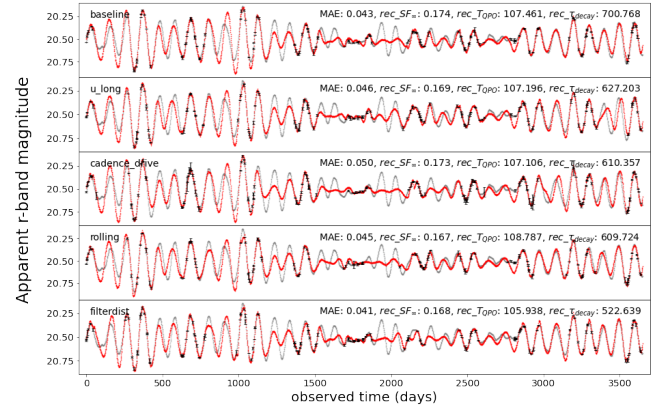
Figure 9. The reconstructions of a quasar with a DRW CARMA process, given in the r-band with the 5 LSST cadences. The original DRW parameter values are $SF_\infty = 0.218$ mag, $\tau = 691.656$ days, and redshift $z = 1.677$. The input light curves are the observed light curves with time dilation considered, which are identical for all five cadences, presented with grey points. Then they are sampled with different cadences respectively, shown in black points with error bars. The reconstructed light curves (by SRNN) are shown with red points. The recovered reconstructed parameters (observed) are given in the top right of each panel. MAE represents the Mean Absolute Error, rec_SF_∞, and rec_τ corresponds to the parameter estimation (by GPR) after reconstruction, which are shown on the top right of each panel.
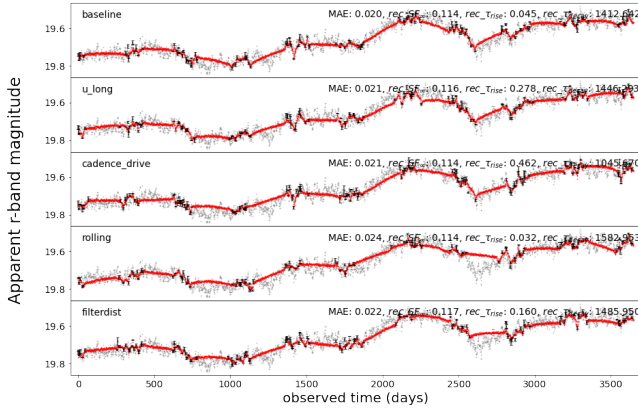
Figure 10. The reconstructions of a quasar with a DHO CARMA process, in the overdamped case. Magnitudes are report in the LSST r-band with the LSST cadences from top panel to bottom panel. The input DHO parameter values are $SF_\infty = 0.215$, $\tau_{\rm rise} = 11.208$ days and $\tau_{\rm decay} = 1118.304$ days. Redshift $z = 1.233$ The reconstructed (observed) DHO parameters are given in the top right of each panel.

trained for the different models (DRW and DHO under/over-damped) separately[16].

Figure 9 presents the reconstructions of a quasar with a DRW CARMA process, given in the r-band with the 5 LSST cadences. The input DRW parameter values are $SF_\infty = 0.218$ mag and $\tau = 691.656$ days, and redshift $z = 1.677$. The input light curve is the same for all five cadences. Figure 10 presents the reconstructions of a quasar with a DHO CARMA process,

<hr>

[16] For input light curves with few observations, it is hard for the SRNN to figure out which case it belongs to.

Figure 11. The reconstructions of a quasar with a DHO CARMA process, in the underdamped case. The input DHO parameter values are $SF_\infty = 0.236$, $\tau_{\rm QPO} = 44.193$ days and $\tau_{\rm decay} = 239.414$days. Redshift $z = 1.372$ The reconstructed (observed) DHO parameters are given in the top right of each panel.

in the overdamped case. The input DHO parameter values are $SF_\infty = 0.215$, $\tau_{\rm rise} = 11.208$ days, $\tau_{\rm decay} = 1118.304$ days, and redshift $z = 1.233$.

The modelling of these two cases shows that SRNN is able to predict the gaps between seasons with stochastic characteristics in general, though it fails to predict accurately the specifics of the variability during the gaps. This is unsurprising, as the CARMA process at each step is indeed a (Gaussian) random variable.

Figure 11 shows the reconstruction of a quasar with a DHO CARMA process in the underdamped case. The input DHO parameter values are $SF_\infty = 0.236$, $\tau_{\rm QPO} = 44.193$ days, $\tau_{\rm decay} = 239.414$ days, and redshift $z = 1.372$. This plot shows that SRNN is better at learning the periodicity characteristic of the DHO-underdamped process. With few observations, SRNN can predict the vacant observations well.

5.2 Parameter estimation analysis

The main motivation of our paper is to investigate whether using a machine learning algorithm on (synthetic) LSST quasar light curve data would be able to detect and/or mitigate any biases in derived CARMA model parameters. Specifically, we have modelled the CARMA(1,0) DRW and CARMA(2,1) DHO processes, the latter in both the over- and underdamped cases. Here we report the results of these investigations.

5.2.1 Metric for CARMA parameters

We design a metric, $M_{\rm err}$, for evaluating how the CARMA parameters are recovered by SRNN-modelled daily light curves, compared with LSST-cadence light curves. This metric is used for the comparisons between combinations of different cadences and bands, and it can also be used as an ensemble metric for each cadence with all bands considered.

$$M_{\rm err} = \frac{1}{N} \sum_i^N \sum_j^M \frac{\left| \theta_{\rm SRNN}^{(i,j)} - \theta_{\rm LSST}^{(i,j)} \right|}{\theta_{\rm in}^{(i,j)}}, \tag{7}$$

where N is the number of light curves used in evaluating the metric. M is the number of parameters for the relevant CARMA model. θ_{SRNN}, θ_{LSST} and θ_{in} are the parameters recovered (by GPR) on the SRNN reconstructed light curves, the parameters recovered from the LSST simulated light curves, and the input parameters, respectively. We calculated the absolute values of differences between θ_{SRNN} and θ_{LSST}, and then divide them with θ_{in} in order to measure each parameter with the same scale. This metric can be extended to any LSST cadences and any bands.

Fig 12 shows our calculated metrics, for each of the five LSST cadences and six LSST bands, in the DRW, DHO-overdamped and DHO-underdamped cases. We also show ensemble metrics for each cadence in each CARMA model. Before metric calculations, those objects with estimated τ_{decay} longer than 10^4 days are regarded as outliers and removed[17].

In this plot, it can be seen that the DHO-underdamped case always gains the lowest M_{err}, as the SRNN algorithm can better simulate this kind of light curve, followed by the DRW case. The DHO-overdamped case always has the largest M_{err}. Regardless of which CARMA model is used, the u-band light curves usually have the largest M_{err}. For most bands, *filterdist* generally has the lowest (best) M_{err}, which shows that the number of observations plays a key role in parameter estimation.

To make this more explicit, the lower right panel of Fig 12 shows ensemble metrics for each cadence. Here three conditions are considered. The mean metric value from all LSST bands in a given cadence shows that the differences between *baseline*, *u_long* and *cadence_drive* are tiny for the DHO-underdamped and DRW models. The *filterdist* cadence always gains the lowest mean M_{err} among all cadences, with *rolling* having the largest value. Such results indicate that *filterdist* might be the optimal cadence for SRNN modelling for this case, and *rolling* is the worst option due to the long gaps in coverage.

However, as the large M_{err} in the u band, which is poorly sampled for most cadences, drives the mean metric to higher values, we also present a mean metric that considers only the five redder bands. In this case, *cadence_drive* gains the lowest metric. If we consider single-band modelling, taking only the minimal value (for any band, but typically r), *u_long*, *cadence_drive* and *filterdist* all perform well, with the best cadence depending on the CARMA model used.

5.2.2 DRW parameters analysis

Finally, we investigate the derived parameters and possible biases in SRNN modelling of AGN, concentrating on the DRW case as it is the most popular model used to analyse AGN time-series. Analysis for DHO cases will be conducted in future work.

Figure 13 shows the trend in recovered timescales compared to the model inputs, expressed as $\log(\rho_{\mathrm{out}})$ and $\log(\rho_{\mathrm{in}})$, where $\rho_{\mathrm{x}} \equiv \tau_{\mathrm{x}}/(10\mathrm{years})$ (the LSST survey length). For small timescales, the recovered τ_{out} from the SRNN-modelled light curves are highly overestimated. This is because a shorter timescale leads to more perturbations within a given gap in

---

[17] LSST only has 10 years observation length, τ much longer than 10 years cannot be estimated correctly.

observations. SRNN shows worse performance in predicting the highly variable magnitudes in longer gaps and fewer observations, resulting in relatively flat predicted light curves and overestimated timescales. For longer timescales, when $\log(\rho) \geqslant -1$, parameter recovery with the SRNN is somewhat better than using the LSST data alone. SRNN-modelled and LSST-cadence metrics almost overlap in r, i, z and y bands. For u band, in all cadences, $\log(\rho_{\mathrm{out}})$ for the SRNN reconstructed light curves is always higher than that for LSST candence light curves.

Examining the ranges of $\log(\rho_{\mathrm{out}})$ for the six bands, the r, z and y bands in all cadences allow the best performance: they are closer to the diagonal than other combinations. Especially for z band, some SRNN metrics at small timescales are very similar to LSST ones. For a given band, the SRNN performance is similar across most cadences, but larger differences are seen in u band – in this case *filterdist* performs relatively better than the others.

Fig 14 shows how well SF_∞ can be recovered from the SRNN-modelled and LSST light curves. It shows that SF_∞ in all bands and cadences are underestimated. When $\log(\mathrm{SF}_{\mathrm{in}})$ increases, $\log(\mathrm{SF}_{\mathrm{out}})$ moves further away from the diagonal. The main reason is a positive correlation between SF_∞ and τ (see Fig 1): high SF_∞ often corresponds to longer timescales, and such light curves require more observation time (time dilation is also considered) to reach the plateau of the SF plot (Fig 3). Given the 10-year LSST survey length, SF_∞ of many objects with long timescales will be underestimated.

In general, the $\mathrm{SF}_{\mathrm{out}}$ distributions from the SRNN and LSST light curves overlap in most cases except for u band. $\mathrm{SF}_{\mathrm{out}}$ estimations from u-band SRNN light curves, with the *baseline*, *u_long*, *cadence_drive* and *rolling* cadences, are lower than those from LSST light curves. This is because light curves with sparse observations make it harder for SRNN to learn their features, resulting in smooth predictions during observing gaps. When more observations are allocated (such as in the *filterdist* cadence), $\mathrm{SF}_{\mathrm{out}}$ gets closer to the diagonal.

6 DISCUSSION

6.1 SRNN modelling performance

Our SRNN model shows the ability to reconstruct realistic AGN light curves for the three CARMA models of interest. However, we have also identified biases and limitations in this method. In particular, the relative inability to predict observations during long gaps means that modelling results are very sensitive to season length and variability timescales, as illustrated in Figures 12, 13, 14.

For normalised timescales $\tau_{\mathrm{in}}/(10\ \mathrm{years}) < 0.1$, the model struggles to capture the damping timescale, with typical fractional errors $\gtrsim 100\%$ (especially in u band). This appears to be less of a problem at large τ_{in}, where parameters inferred from the SRNN are at least as accurate as those measured directly from the LSST-cadence light curves (Fig 13).

The model performs better in recovering the structure function. As shown in Fig 14, this can be recovered as accurately from the SRNN light curves as from the LSST light curves, in all bands except u, where the lower number of detections likely inhibits SRNN reconstruction. Interestingly, the recovered values of SF_∞ are systematically slightly below the input values for both SRNN and LSST light curves.

Metric Statistics for SRNN Modelling
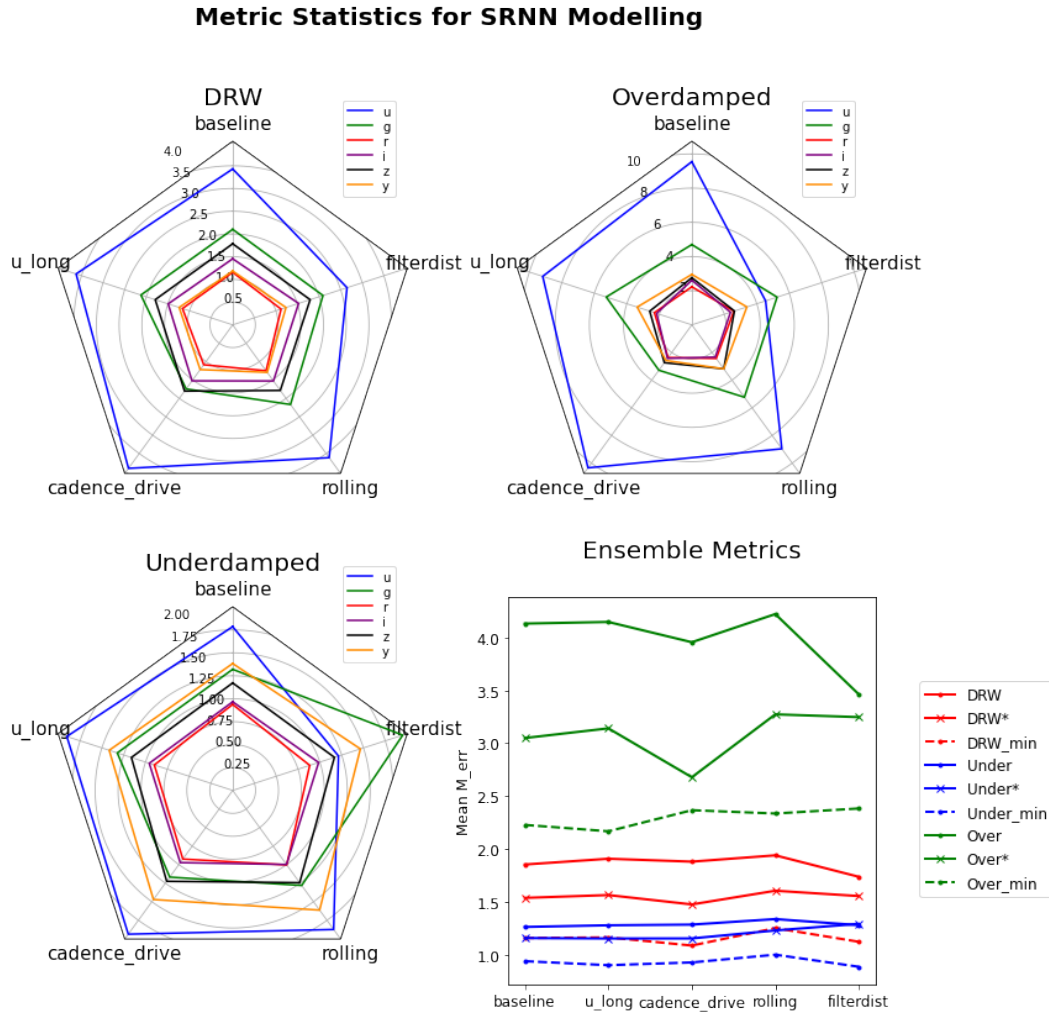
Figure 12. CARMA Metric under different LSST cadences. Upper left, upper right and lower left subplots show the metrics with DRW, DHO-overdamped and DHO-underdamped cases, respectively. The lower right subplot shows the ensemble metric for different CARMA cases and cadences. The solid lines with round markers correspond to the mean value with each cadence; The solid lines with 'x' marker (The labels with *) correspond to the mean value without *u* band; The dashed lines correspond to the minimal value for any band (usually *r*) within each cadence.

6.2 Comparisons with previous work

The range of ML techniques is vast and here we concentrate on five main artificial neural network types: the Recurrent Neural Network (RNN), the Recurrent Autoencoder (RAE), the Variational Recurrent Autoencoder (VRAE), the Variational RNN (VRNN) and the Stochastic Recurrent Neural Network (SRNN). Very high-level descriptions of these four architectures and astronomical applications are given in Table 6. We also compare the motivations, input formats, architecture and results of Tachibana et al. (2020); Sánchez-Sáez et al. (2021) and this paper, shown in Table 7.

Our study represents the first application of an SRNN to astronomical research. The unique design of the SRNN is to stack a SSM layer on the traditional RNN layer in order to learn and produce both the underlying features and corresponding stochastic fluctuations. SRNN is suitable for modelling light curves with extremely high variability, especially AGN. Given an AGN, when dense observations and uniform cadences are provided, SRNN can learn its features

better. However, SRNN also has some weaknesses. Its input and output sequence lengths should always be identical, and its forecasting ability is relatively weak since the behaviour is inherently random. Nonetheless, given its ability to reconstruct realistic AGN light curves, we encourage further investigations regarding its architecture.

6.3 Implications in LSST

Our research is expected to help the LSST AGN collaboration to consider optimal cadences for studying AGN variability. To investigate this, we examined the results of our metric evaluation (Eq 7) for each LSST band under various classes of proposed LSST cadence (Fig 12). For existed cadence strategies, we conclude that *filterdist* is the best cadence for band-averaged case. As *u* band always has the worst score due to the fewest total observations, we also only consider a metric with only *g*, *r*, *i*, *z* and *y* bands, and find that *cadence_drive* is favoured in this case. If we just look at the 'best' band case, *u_long* is slightly better than *baseline* and *cadence_drive*.
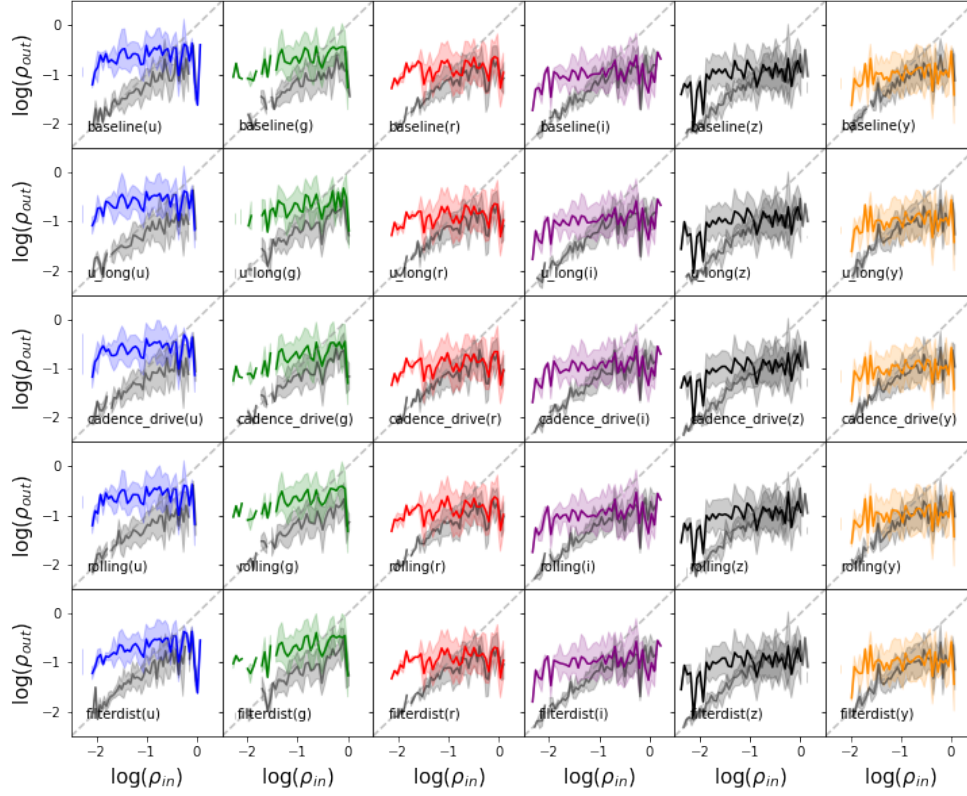
Figure 13. τ estimation for DRW processes. ρ_{in} and ρ_{out} are defined as τ_{in} (the input timescale) and τ_{out} (the recovered timescale from the simulated SRNN or LSST data) divided by 10 years (the LSST survey observation length). Each row corresponds to a different LSST cadence, and each column corresponds to a band. Results from the SRNN-modelled light curves are shown with colours, and results from LSST-cadence light curves are shown in grey. The shaded areas indicate the standard deviation around the median, in 50 bins in ρ_{in}, following outlier rejection.

However, our experiments show that SRNN performs better for uniformly-seasonal light curves (see Fig 8) with denser detections, which is reasonable as with more information provided for the SRNN, it can learn the underlying features more easily. Therefore, it might perform better for the Deep Drilling Fields (DDF), where the cadences are more dense and uniform compared to the WFD survey.

6.4 SRNN forecasting

Forecasting future light curve behaviour for a given object is another goal of applying machine learning to AGN. We tried to use SRNN for forecasting, and tested its ability to predict one or several steps for one run and fold the outputs as the input for the next run, and to predict a length of future light curves for one run. However, the results are not promising: our SRNN can only predict light curves for about one month, with low accuracy. As time increases, the error gets bigger and light curves become increasingly flat. This suggests that the SRNN architecture may not be suitable for forecasting, due to its non-deterministic (random) nature. More experiments will be done in the future.

7 CONCLUSIONS

Cadence strategy plays an important role in light curve modelling, especially for AGN with long timescales and high variability features. This paper introduces a Stochastic Recurrent Neural Network (SRNN) to model realistic LSST-cadence light curves simulated using CARMA models, and provides a quantitative metric to evaluate and compare the performance between five selected LSST cadence strategies.

In this study, we:

• Investigated the popular CARMA models, which are often applied in AGN light curve simulations. In addition to the usual Damped Random Walk model, we also explored Damped Harmonic Oscillator models (underdamped and overdamped cases), which may be more applicable to some AGN.

• Designed a *QuasarMetric* for simulating LSST-cadence light curves (MJD, mag, σ_{mag}) given varying input CARMA parameters.

• Applied modified Stochastic Recurrent Neural Networks to AGN light curve modelling, to achieve stochastic modelling and prediction

• Provided a metric, M_{err}, for estimating how well SRNN can help recover the input parameters with Gaussian Process Regression, compared with pure LSST-cadence light curves.

• Concluded that *filterdist*, *cadence_drive* and *u_long* strategies are the optimal when six bands, five bands, and the best band are considered, respectively.
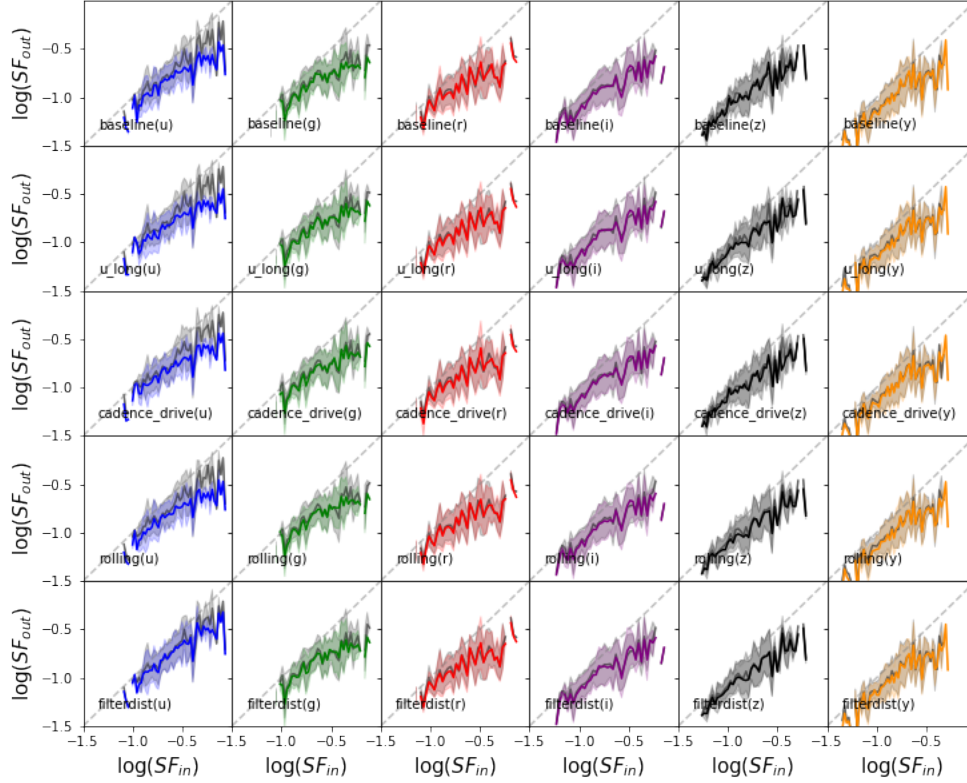
Figure 14. Same as Fig 13 but for SF_∞. SF_{in} and SF_{out} are the real SF_∞ and estimated SF_∞ from SRNN or LSST light curves, respectively. The fitting lines with colours are for metrics of SRNN-modelled light curves, and the grey ones are for LSST light curves.

This research provides a method for quantifying the performance for AGN science of any potential LSST cadence strategies. We expect our research may help LSST community to measure and select proper cadence for the WDF field.

Data Availability
The code and simulated data underlying this article are available at https://github.com/XinyueSheng2019/LSST_AGN_SRNN_Paper.

APPENDIX A: THE CARMA(1,0) AND CARMA(2,1) MODELS

A0.1 CARMA in a nutshell

Kelly et al. (2014) and Moreno et al. (2019) show the detailed introduction of CARMA in different dimensions. Here, we would like to extract the key information from them, which are beneficial for our research.

CARMA(X, Y) is derived from discrete ARMA model,

which is applied to ... Equation A1 is the CARMA equation (from Equation (1) in Kelly et al. (2014)).

$$\frac{d^p y(t)}{dt^p} + \alpha_{p-1}\frac{d^{p-1}y(t)}{dt^{p-1}} + ... + \alpha_0 y(t) =$$
$$\beta_q \frac{d^q \epsilon(t)}{dt^q} + \beta_{q-1}\frac{d^{q-1}\epsilon(t)}{dt^{q-1}} + ... + \epsilon(t)$$

(A1)

The left-side of the equation with C-AR coefficients α describes the auto-regressive part of the system; the right-side describes the driving perturbation C-MA. In our work, we only focus on DRW - CARMA(1,0) and DHO - CARMA(2,1). Table A1 shows all relevant equations about DRW and DHO, followed by notation explanation in Table A2.

APPENDIX B: STOCHASTIC RECURRENT NEURAL NETWORK

B1 The Evidence Lower Bound (ELBO)

Maximizing $\mathcal{F}$ is the equivalent of maximzing the (log) likelihood, $p(x|z)$, and minimizing the distance to the prior, $D_{KL}(q(z) \| p(z|x))$.

KL divergence is always equal to, or greater than 0. Hence the ELBO is always below the (log) evidence of our data and in that sense it is the lower bound: $\mathcal{F}(\theta, \phi) = \sum_i \mathcal{F}_i(\theta, \phi) \le \mathcal{L}(\theta)$.

The KL divergence is for measuring the differences between two probability distributions. In this research, it is applied to measure the differences between prior and posterior z

ML network	Description	Recent astrophysics studies
Recurrent Neural Network (RNN)	RNN uses multiple layers of recurrent cells (RNN, GRU, LSTM, etc) for processing sequential data. Connections between nodes form a directed graph along a temporal sequence.	Dékány & Grebel (2020), Fremling et al. (2021), Burhanudin et al. (2021)
Recurrent AutoEncoder (RAE)	Its encoder learns a representation (encoding) for a set of data, typically for dimensional reduction (2D time sequences to 1D latent variables), by training the network to extract the inherent features from input sequences, and ignore insignificant or noisy data. Then, the representation, or so-called 1D latent variables are fed into a decoder, which decodes the features and generate output sequences. This architecture is design for sequence modelling and forecasting.	Naul et al. (2018), Tsang & Schultz (2019), Jamal & Bloom (2020), Tachibana et al. (2020), Villar et al. (2021)
Variational Recurrent Autoencoder (VRAE)	Similar to RAE that it consists of an encoder that learns a mapping from input sequences to latent representation, and a decoder mapping from the latent representation to outputs. However, the Variational approach maps the data to *Gaussian distributions* of latent variables instead of determined variables. Such design provide flexibility for VRAE to generate new and varying outputs with similar features.	Sánchez-Sáez et al. (2021)
Variational RNN (VRNN)	VRNN contains a Variational Auto-Encoder (VAE) at each step, and each VAE (including the prior of the latent random variables) is dependent on the hidden state at the previous step h_{t-1}.	*None*
Stochastic Recurrent Neural Network (SRNN)	Extended from VRNN, SRNN model combines both VRNN and SSM (state space model) advantages. Compared with VRNN generating deterministic values, SRNN provides stochastic random variables sampled from latent Gaussian distributions, thus more suitable for time-series study with high variability.	*this paper*

Table 6. A very high-level descriptions of the four architectures most discussed in this paper.

distributions. For one pair of input and output sequences, the calculation is shown in Equation B1.

$$
\begin{aligned}
D_{\mathrm{KL}}(q(z) \parallel p(z|x)) &= \int_z q(z) \log \frac{q(z)}{p(z|x)} dz \\
&= \mathbb{E}_{z \sim q}[\log q(z)] - \mathbb{E}_{z \sim q}[\log p(z|x)]
\end{aligned} \quad \text{(B1)}
$$

B2 SRNN Implementation

There is no simple command to invoke the SRNN in TensorFlow. Instead, as described in Section 4.1, the SRNN is built with a Generative Model and an Inference Model. This is implemented for our study as follows:

```
########### Generative Model ############
## two h layers
X_inputs = Input(shape = (timestep, features), name =
    'X_input')
h1_out = Bidirectional(GRU(num_neutron, name = 'h_0',
    return_sequences=True))(X_inputs)
h1_out = Bidirectional(GRU(num_neutron, name = 'h_0',
    return_sequences=True))(d1_out)

## Bidirectional wrapper for RNN;
## generate prior z from h1
```

```
prior_z_mean  = Bidirectional(GRU(z_neutron, name =
    'prior_mean', return_sequences=True))(h1_out)
prior_z_log_var = Bidirectional(GRU(z_neutron, name =
    'prior_log_var', return_sequences=True))(h1_out)
prior_sampled_z = Sampling(name =
    'sampling_prior')([prior_z_mean, prior_z_log_var])
merged_prior = concatenate([h1_out, prior_sampled_z])

## prior_outputs will be the real outputs for validation
    set
prior_outputs = TimeDistributed(Dense(1),
    name='time_dist')(merged_prior)

generative_model = Model(X_inputs, [prior_outputs,
    prior_z_mean, prior_z_log_var, h1_out], name =
    'generative_model')


########### Inference Model ###########
## reverse layer a for inference
g1_out  = Input(shape = (pred_timestep, num_neutron*2),
    name = 'g1_out')
Y_inputs = Input(shape = (pred_timestep, pred_features),
    name = 'Y_input')
merged_input = concatenate([g1_out, Y_inputs])
# Reversed Layer, a
a_out = Bidirectional(GRU(num_neutron, name = 'a_0',
    return_sequences=True,
    go_backwards=True))(merged_input)
```

Table 7. Comparison between machine learning applications to AGN in Tachibana et al. (2020), Sánchez-Sáez et al. (2021), and *this paper*.

Attribute	Tachibana et al. (2020)	Sánchez-Sáez et al. (2021)	*this paper*
Motivation	Focus on how well RAE learns the underlying processes and achieve modelling and forecasting of the general trend, rather than the stochasticity.	Aim to recognize changing-look AGN by modelling its light curves with VRAE and obtain their general behaviours and features.	Model the whole 10-year light curves and predict the vacancies and stochastic features, thus helping LSST cadence strategies evaluation.
Input format	Normalized mags and mag_errors, Δt	Normalized mags and mag_errors, Δt	Normalized mags and mag_errors, at each timestep with vacancies (filled with zeros) at some timesteps
Architecture	Recurrent Auto-encoder.	Variational Recurrent Auto-encoder.	Stochastic Recurrent Neural Networks.
Key results	Modeled light curves from the Zwicky Transient Facility data release 5 (ZTF DR5) with a VRAE architecture obtaining a set of attributes from the VRAE latent space that describes the general behaviour of the data. These attributes are used as features for an anomaly detector. These anomalies are dominated by bogus candidates, Identify 75 promising Changing-State AGN candidates.	Applied a Recurrent Neural Network Auto-encoder (AE) to model and predict quasar variability and reported that the auto-encoder showed better performance than DRW modelling in forecasting short-term variability. Additionally, they found temporal asymmetry in the optical variability, and the decrease of the amplitude of the variability asymmetry as the luminosity and/or black hole mass increases.	Applied SRNN to model simulated LSST-cadence AGN light curves, learn the stochasticity and latent features, and eventually recover their daily light curves. Provided a metric M_{err} to quantify the influence of different LSST cadence strategies on CARMA parameter recovery.

```
posterior_z_mean  = Bidirectional(GRU(z_neutron, name =
    'posterior_z_mean', return_sequences=True,
    go_backwards=True))(a_out)
posterior_z_log_var = Bidirectional(GRU(z_neutron, name
    = 'posterior_z_log_var', return_sequences=True,
    go_backwards=True))(a_out)

inference_model = Model([g1_out, Y_inputs],
    [posterior_z_mean, posterior_z_log_var], name =
    'inference_model')

## Fulfilling the SRNN
srnn = SRNN(generative_model, inference_model)
```

References

Abazajian K. N., et al., 2009, ApJS, 182, 543

Ai Y. L., Yuan W., Zhou H. Y., Wang T. G., Dong X. B., Wang J. G., Lu H. L., 2010, ApJ, 716, L31

Annis J., et al., 2014, ApJ, 794, 120

Becker I., Pichara K., Catelan M., Protopapas P., Aguirre C., Nikzat F., 2020, MNRAS, 493, 2981

Boone K., 2019, AJ, 158, 257

Brockwell P. J., Davis R. A., 2002, Introduction to Time Series and Forecasting. Springer-Verlag New York

Burhanudin U. F., et al., 2021, arXiv e-prints, p. arXiv:2105.11169

Butler N. R., Bloom J. S., 2011, AJ, 141, 93

Cai Z.-Y., Wang J.-X., Gu W.-M., Sun Y.-H., Wu M.-C., Huang X.-X., Chen X.-Y., 2016, The Astrophysical Journal, 826, 7

Charnock T., Moss A., 2017, ApJ, 837, L28

Chung J., Kastner K., Dinh L., Goel K., Courville A., Bengio Y., 2016, A Recurrent Latent Variable Model for Sequential Data (arXiv:1506.02216)

Czerny B., Janiuk A., Rózańska A., Zycki P. T., 1999, in Poutanen J., Svensson R., eds, Astronomical Society of the Pacific Conference Series Vol. 161, High Energy Processes in Accreting Black Holes. p. 331

Dékány I., Grebel E. K., 2020, ApJ, 898, 46

Dexter J., Agol E., 2011, ApJ, 727, L24

Dexter J., Begelman M. C., 2018, Monthly Notices of the Royal Astronomical Society: Letters, 483, L17

Edelson R., Vaughan S., Malkan M., Kelly B. C., Smith K. L., Boyd P. T., Mushotzky R., 2014, ApJ, 795, 2

Escamilla-Rivera C., Carvajal Quintero M. A., Capozziello S., 2020, J. Cosmology Astropart. Phys., 2020, 008

Fabius O., van Amersfoort J. R., 2015, Variational Recurrent Auto-Encoders (arXiv:1412.6581v6)

Feigelson E. D., Babu G. J., Caceres G. A., 2018, Frontiers in Physics, 6, 80

Foreman-Mackey D., Agol E., Ambikasaran S., Angus R., 2017, The Astronomical Journal, 154, 220

Fraccaro M., Sønderby S. K., Paquet U., Winther O., 2016, Sequential Neural Models with Stochastic Layers (arXiv:1605.07571)

Fremling C., et al., 2021, arXiv e-prints, p. arXiv:2104.12980

Fukugita M., Ichikawa T., Gunn J. E., Doi M., Shimasaku K., Schneider D. P., 1996, AJ, 111, 1748

Greenstein J. L., 1963, Nature, 197, 1041

Hazard C., Mackey M. B., Shimmins A. J., 1963, Nature, 197, 1037

Hinners T. A., Tat K., Thorp R., 2018, AJ, 156, 7

Hložek R., et al., 2020, arXiv e-prints, p. arXiv:2012.12392v1

Howell S. B., et al., 2014, PASP, 126, 398

Ivezic Z., 2016, Proceedings of the International Astronomical Union, 12, 330–337

Ivezić Ž., et al., 2019, ApJ, 873, 111

Jamal S., Bloom J. S., 2020, The Astrophysical Journal Supplement Series, 250, 30

Jiang Y.-F., Blaes O., 2020, ApJ, 900, 25

Jiang Y.-F., Blaes O., Stone J. M., Davis S. W., 2019, ApJ, 885,

CARMA	DRW-CARMA(1,0)	DHO-CARMA(2,1)
Differential Equation	$d^1 x + \alpha_1 x(t) = \beta_0 dW(t)$ $dX(t) = -\frac{1}{\tau} X(t) dt + \sigma \sqrt{dt}\epsilon(t) + b dt$ where $\tau, \sigma, t > 0$	$d^2 x + \alpha_1 d^1 x + \alpha_2 x = \beta_0(dW) + \beta_1 d^1(dW)$
State-space model	$x(t+\delta t) = e^{\alpha_1 \delta t} x(t) + \beta_0 \int_0^{\delta t} e^{\alpha_1(\delta t - s)} dW_s$	$x(t+\delta t) = e^{\alpha_1 \delta t} x(t) + e^{\alpha_2 \delta t} x(t) + \int_0^{\delta t} e^{A(\delta t - s)} B dW_s,$ $A = \begin{bmatrix} -\alpha_1 & 1 \\ -\alpha_2 & 0 \end{bmatrix}, B = [\beta_1, \beta_0]^T$
Input Parameters	$\tau_{\text{decay}} = -\frac{1}{r_1} = \frac{1}{\alpha_1}$ $\sigma = \beta_0^2$	$\tau_{\text{blue}} = \left\| \frac{\beta_1}{\beta_0} \right\|$ $\sigma_{lc}^2 = ACVF(0) = \sigma_{Noise}^2 \frac{\beta_0^2 + \beta_1^2 \alpha_2}{2\alpha_1 \alpha_2}$ Overdamping: $\tau_{\text{rise}} = \frac{1}{r_2 - r_1} ln \left\| \frac{r_1}{r_2} \right\| \approx \left\| \frac{1}{min(r_1,r_2)} \right\|$ $\tau_{\text{decay}} = \left\| \frac{1}{max(r_1,r_2)} \right\|$ Underdamped: $\omega_n = \sqrt{\alpha_2}$ $\omega_d = \omega_n \sqrt{1 - \xi^2} = \sqrt{\alpha_2 - \frac{\alpha_1^2}{4}}$ $\xi = \frac{\alpha_1}{2\sqrt{\alpha_2}}$ $\tau_{\text{QPO}} = \left\| \frac{2\pi}{\omega_n} \right\|$ $T_{\text{dQPO}} = \left\| \frac{2\pi}{\omega_d} \right\|$ $\tau_{\text{decay}} = \left\| \frac{1}{\mathscr{R}(r_1)} \right\| = \left\| \frac{1}{\mathscr{R}(r_2)} \right\| = \left\| \frac{2}{\alpha_1} \right\|$
Impulse Response	$d^1 G + \alpha_1 G = \delta(t)$ $G(t) = C e^{-\alpha_1 t}$	$G + \alpha_1 d^1 G + \alpha_2 G = \delta(t)$ $G(t) = C_1 e^{r_1 t} + C_2 e^{r_2 t}$ $\begin{bmatrix} r_1 & r_2 \\ 1 & 1 \end{bmatrix} \begin{bmatrix} C_1 \\ C_2 \end{bmatrix} = \begin{bmatrix} 1 \\ 0 \end{bmatrix}$
Auto-correlation function	$ACF(\Delta t) = e^{-\frac{\|\Delta t\|}{\tau}}$	$ACVF(\Delta t) = C_0 (C_1 e^{r_1 \Delta t} + C_2 e^{r_2 \Delta t})$ $ACF(\Delta t) = \frac{ACVF(\Delta t)}{ACVF(0)}$ $C_0 = \frac{\sigma_{Noise}^2}{2(r_2 - r_1)}$ $C_1 = -\frac{\beta_0^2 - \beta_1^2 r_1^2}{\mathscr{R}(r_1)(r_1 + r_2^*)}$ $C_2 = \frac{\beta_0^2 - \beta_1^2 r_2^2}{\mathscr{R}(r_2)(r_2 + r_1^*)}$
Structure Function	$SF(\Delta t) = SF_\infty (1 - e^{-\|\Delta t\|/\tau})^{1/2}, SF_\infty = \sqrt{2}\sigma$	$SF(\Delta t) = \sqrt{2(ACVF(0) - ACVF(\Delta t))}$
Power Spectra Density	$p(f) = \frac{\beta_0^2}{\alpha_1 + (2\pi f)^2}$	$p(f) = \frac{1}{2\pi} \frac{\beta_0^2 + 4\pi^2 \beta_1^2 f^2}{16\pi^4 f^4 + 4\pi^2(\alpha_1^2 - 2\alpha_2) f^2 + \alpha_2^2}$

Table A1. Summary of the key DRW and DHO equations (Moreno et al. 2019; Kasliwal et al. 2017; Kelly et al. 2009, 2014). For the right-hand-side (RHS) of each differential equation, $\epsilon(t)$ corresponds to a white noise process with the mean equal to zero and variance (σ_{Noise}^2) equal to one (Kelly et al. 2009). For DRW, there is only one root, r_1, which is equal to $-\alpha_1$. For DHO, the r_1 and r_2 mean the two roots of characteristic equations for the left-hand-side (LHS) of each differential equation. These could be real or complex, corresponding to overdamped and underdamped cases, respectively. Further symbols are defined in Table A2.

144

Jones R. L., et al., 2014, in Peck A. B., Benn C. R., Seaman R. L., eds, Society of Photo-Optical Instrumentation Engineers (SPIE) Conference Series Vol. 9149, Observatory Operations: Strategies, Processes, and Systems V. p. 91490B, doi:10.1117/12.2056835

Kasliwal V. P., Vogeley M. S., Richards G. T., 2015, MNRAS, 451, 4328

Kasliwal V. P., Vogeley M. S., Richards G. T., 2017, MNRAS, 470, 3027

Kelly B. C., Bechtold J., Siemiginowska A., 2009, ApJ, 698, 895

Kelly B. C., Becker A. C., Sobolewska M., Siemiginowska A., Uttley P., 2014, ApJ, 788, 33

Kessler R., et al., 2019, Publications of the Astronomical Society

of the Pacific, 131, 094501

Kingma D. P., Welling M., 2014, Auto-Encoding Variational Bayes (arXiv:1312.6114)

Kovacevic A., Ilic D., Jankov I., Popovic L. C., Yoon I., Radovic V., Caplar N., Cvorovic-Hajdinjak I., 2021a, arXiv e-prints, p. arXiv:2105.12420

Kovacevic A. B., et al., 2021b, arXiv e-prints, p. arXiv:2105.14889

Kovačević A. B., Popović L. Č., Ilić D., 2020, Open Astronomy, 29, 51

Kozłowski S., 2016a, MNRAS, 459, 2787

Kozłowski S., 2016b, ApJ, 826, 118

Kozłowski S., 2017, Astronomy & Astrophysics, 597, A128

Kozłowski S., et al., 2010, ApJ, 708, 927

DRW	
τ	The characteristic/decay timescale. Represents the time for the time series to become uncorrelated.
SF_∞	The long-term variability, $\mathrm{SF}_\infty = \sqrt{2}\sigma$.
σ	the long-term standard deviation of variability, independent of τ and observation length, however, when the observation length is much longer than τ, the variance of time series will be very close to σ.
$\hat{\sigma}$	$\hat{\sigma} = \mathrm{SF}_\infty/\sqrt{\tau} = \sqrt{2}\sigma/\sqrt{\tau}$
	For $\Delta t \ll \tau$ the dispersion between two points is $\hat{\sigma}\,|\Delta t|^{1/2}$;
	for $\Delta t \gg \tau$, the dispersion asymptotes to σ (Kozłowski et al. 2010).
dW & $\epsilon(t)$	Proved by Ito's theorem Thomas (1986), Wiener increments dW and random variable $\epsilon(t)$ are equivalent.
DHO	
α_1	First coefficient of Continuous-AR
α_2	Second coefficient of Continuous-AR, equal to ω^2
β_0	First coefficient of Moving Average equation
β_1	Second coefficient of Moving Average equation
τ_{decay}	Decay timescale for DHO.
τ_{rise}	Rise timescale for overdamped DHO. It is a feature in Green's function showing the time corresponding to the peak value. When $\tau_{\mathrm{rise}} = 0$, it becomes DRW.
τ_{blue}	The ratio of $\left|\frac{\beta_1}{\beta_0}\right|$. As τ_{blue} increases, the time series becomes more erratic.
ω_n	Natural quasi-periodic oscillation (QPO) frequency
ω_d	Decay QPO frequency
τ_{QPO}	Period of natural QPO frequency
T_{dQPO}	Period of decay QPO frequency
	Damping ratio of the oscillator, equal to $\frac{\alpha_1}{2\sqrt{\alpha_2}}$.
ξ	$\xi > 1$, it is an overdamped DHO;
	$\xi = 1$, it is a critical damped DHO;
	$\xi < 1$ it is an underdamped DHO.

Table A2. Key parameters in the DRW and DHO models.

Kubota A., Done C., 2018, MNRAS, 480, 1247

Kullback S., Leibler R. A., 1951, The Annals of Mathematical Statistics, 22, 79

LSST Science Collaboration et al., 2009, arXiv e-prints, p. arXiv:0912.0201

LSST Science Collaboration et al., 2017, arXiv e-prints, p. arXiv:1708.04058

Lin Y.-C., Wu J.-H. P., 2021, Phys. Rev. D, 103, 063034

Lochner M., et al., 2021, arXiv e-prints, p. arXiv:2104.05676

Lyke B. W., et al., 2020, ApJS, 250, 8

MacLeod C. L., 2012, PhD thesis, University of Washington

MacLeod C. L., et al., 2010, The Astrophysical Journal, 721, 1014â€"1033

Matthews T. A., Sandage A. R., 1963, ApJ, 138, 30

Meusinger H., Hinze A., de Hoon A., 2011, A&A, 525, A37

Möller A., de Boissière T., 2020, MNRAS, 491, 4277

Moreno J., Vogeley M. S., Richards G. T., Yu W., 2019, Publications of the Astronomical Society of the Pacific, 131, 063001

Muthukrishna D., Narayan G., Mandel K. S., Biswas R., Hložek R., 2019, PASP, 131, 118002

Naul B., Bloom J. S., Pérez F., van der Walt S., 2018, Nature Astronomy, 2, 151

Oke J. B., 1963, Nature, 197, 1040

Oke J. B., Gunn J. E., 1983, ApJ, 266, 713

Peterson B. M., Horne K., 2004, Astronomische Nachrichten, 325, 248â€"251

Press W. H., 1978, Comments on Astrophysics, 7, 103

Rasmussen C. E., Williams C. K. I., 2006, Gaussian processes for machine learning.. Adaptive computation and machine learning, MIT Press

Richards G. T., et al., 2001, AJ, 121, 2308

Rybicki G. B., Press W. H., 1995, Phys. Rev. Lett., 74, 1060

Sánchez-Sáez P., et al., 2021, arXiv e-prints, p. arXiv:2106.07660

Schmidt M., 1963, Nature, 197, 1040

Schmidt F., Hofmann T., 2018, Deep State Space Models for Unconditional Word Generation (arXiv:1806.04550)

Schmidt K. B., Marshall P. J., Rix H.-W., Jester S., Hennawi J. F., Dobler G., 2010, ApJ, 714, 1194

Sesar B., et al., 2007, AJ, 134, 2236

Shakura N. I., Sunyaev R. A., 1973, A&A, 500, 33

Suberlak K. L., Ivezić Ž., MacLeod C., 2021, ApJ, 907, 96

Tachibana Y., Graham M. J., Kawai N., Djorgovski S. G., Drake A. J., Mahabal A. A., Stern D., 2020, The Astrophysical Journal, 903, 54

Tarnopolski M., Żywucka N., Marchenko V., Pascual-Granado J., 2020, ApJS, 250, 1

Thomas A., 1986, Journal of Physics A Mathematical General, 19, 929

Tsang B. T.-H., Schultz W. C., 2019, The Astrophysical Journal, 877, L14

Vanden Berk D. E., et al., 2004, ApJ, 601, 692

Villar V. A., Cranmer M., Berger E., Contardo G., Ho S., Hosseinzadeh G., Yao-Yu Lin J., 2021, arXiv e-prints, p. arXiv:2103.12102

Wilhite B. C., Vanden Berk D. E., Kron R. G., Schneider D. P., Pereyra N., Brunner R. J., Richards G. T., Brinkmann J. V., 2005, ApJ, 633, 638

Williams J., Carini M. T., 2015, in American Astronomical Society Meeting Abstracts #225. p. 144.56

Yin Z., Barucca P., 2021, Stochastic Recurrent Neural Network for Multistep Time Series Forecasting (arXiv:2104.12311)

This paper has been typeset from a TEX/LATEX file prepared by the author.